Title

Structure-Property Relationships of A992 Structural Steels

Permalink

https://escholarship.org/uc/item/3dq266vh

Author

Peng, Hexuan

Publication Date

2021

Peer reviewed|Thesis/dissertation

UNIVERSITY OF CALIFONIA SAN DIEGO

Structure-Property Relationships of A992 Structural Steels

A thesis submitted in partial satisfaction of the
requirements for the degree
Master of Science

in

Materials Science and Engineering

by

Hexuan Peng

Committee in charge:

Professor Machel Morrison, Chair
Professor Michael Frazier
Professor Yu Qiao

2021

The thesis of Hexuan Peng is approved, and it is acceptable in quality and form for publication on microfilm and electronically.

University of California San Diego

2021

TABLE OF CONTENTS

LISY OF FIGURES

LIST OF TABLES

Acknowledgements

It is a great honor for me to have worked with Professor Machel Morrison during the past two quarters. I would like to thank him for his patience and extraordinary guidance of this research project. I also want to thank Sabine Faulhaber, Dr. Stephen Horvath and Professor Kenneth Vecchio for their research advice and technical discussion. Finally I would like to thank my parents to fund my master degree and always have confidence in me.

ABSTACT OF THE THESIS

Structure-Property Relationships of A992 Structural Steels

by

Hexuan Peng

Master of Science in Materials Science and Engineering

University of California San Diego, 2021

Professor Machel Morrison, Chair

Adopting a material-level architecture gives engineers an additional tool in structural design. The exploitation of the material architecture can produce efficient and effective seismic force resisting systems. Examples of this include utilizing novel materials or functionally graded materials for constructing members with spatial variation in strength, and stiffness. This approach can be used to enforce capacity design principles; increase energy dissipation; and prevent premature component and demand critical connection failures. Recently heat-treatment has been proposed as a method to selectively reduce the strength of steel members to form weak zones with high ductility and energy absorption capabilities. So far, the method has been applied to beams in special moment frames and braces and gusset plates in special concentrically braced frames. However, no recommendations have been put forward as to the details of the heat treatment process required to achieve the desired material properties. Therefore, in this study the structure property relationships of one of the commonly used structural steel grades (ASTM A992 steel) is investigated with the goal of establishing relationships between heat treatment process and resulting steel strength.

The dependence of microstructural features of these steels, including grain sizes and phase volume fractions, on heat treatments and chemical compositions is investigated.

A992 steels with different chemical composition were selected and heat treated in different ways. After that, their microstructural and mechanical properties were characterized by optical microscope, electron back-scatter diffraction, energy-dispersive X-ray spectroscopy and standard mechanical tests.

The austenite grain coarsening behavior upon heating, was investigated under different heating conditions, involving peak temperature and holding time. The dependence of ferrite grain size on prior austenite grain size and cooling rate has also been studied. In addition, the strengthening contributions of grain boundaries, solutes, dislocations and precipitates to the overall strength of the steel are evaluated in a quantitative manner. Finally, an empirical model for the prediction of yield strength of A992 steels was developed based on the existing

experimental data.

Chapter 1

Background and motivation

One of the seismic design philosophies for civil engineering structures like bridges and buildings is capacity design. Capacity design is a design process in which it is decided which objects elements within a structural system will be permitted to yield (ductile components) and which objects will remain elastic (brittle components) in the event of a structural overload (i.e. loading the structure beyond its elastic limit). Enhancing the overall energy dissipation capacity and ductility of the structure is usually the guiding principle used when deciding which elements are to be "ductile components" and which are to be "brittle components" is typically.

Once this decision is made, design proceeds according to the following guidelines: Ductile components are designed with sufficient deformation capacity such that they may satisfy the estimated displacement demands and brittle components are designed to achieve sufficient strength levels such that they may satisfy strength-based demand-capacity ratios. These brittle components are therefore referred to as "capacity protected" elements and are protected against failure, by providing them with a strength greater than that corresponding to the development of the maximum feasible strength in the ductile components[1].

The selection of structural members in a moment resisting building in a region of high seismicity, as an example, will have beams as the horizontal members rigidly connected to columns as the vertical members. Beams directly support the floors slabs and the columns support the beams. When capacity design is applied to such a building system, we select the members to fit in one of the two categories. One is the capacity protected element (sometimes also called force-controlled element), and the other type is the ductile element (sometimes called deformation-controlled element or energy dissipative element)[1].

The process begins with picking the ductile elements, and then detailing them (which i.e. picking the size, the material, the geometry and their connections) in such a way that they are able to yield, dissipate energy and resist seismic forces in the event of a structural overload (large earthquake). When these elements yield, they will typically work harden until they achieve a peak (or ultimate) strength or resistance. The designer, therefore, must determine this peak strength and then design the force-controlled elements to remain nominally elastic at these force levels. Therefore, force-based elements are designed to resist the capacity of the ductile elements which can be much greater than the seismic design forces[2, 3].

The capacity design concept for buildings experiencing a large earthquake is analogous to the crash safety design of a motor car. During a head on collision for example, the structural elements of the car are designed to yield and, absorb the kinetic energy of the vehicle in order to protect the passengers. The design of the car in this way is more practical and economical than if the car were designed to remain completely elastic during a crash. This concept is similar to the design of a building to withstand a large earthquake. The building is designed to allow ductile yielding (or other forms of damage such as buckling) at specific predictable locations within the structure to prevent structural collapse and life loss.

In traditional reinforced concrete and steel moment frame buildings, yielding and plastic hinging of the beams at their ends and at the column based is the desired distribution of damage as it results in a very ductile response of the structure. This mode of structural damage or failure is sometimes called a sway mechanism (Fig 1.5) and is in direct contrast to a soft story mechanism in which hinges form in the columns at the top and bottom of a single story. This failure mode is shown in Fig 1.2.

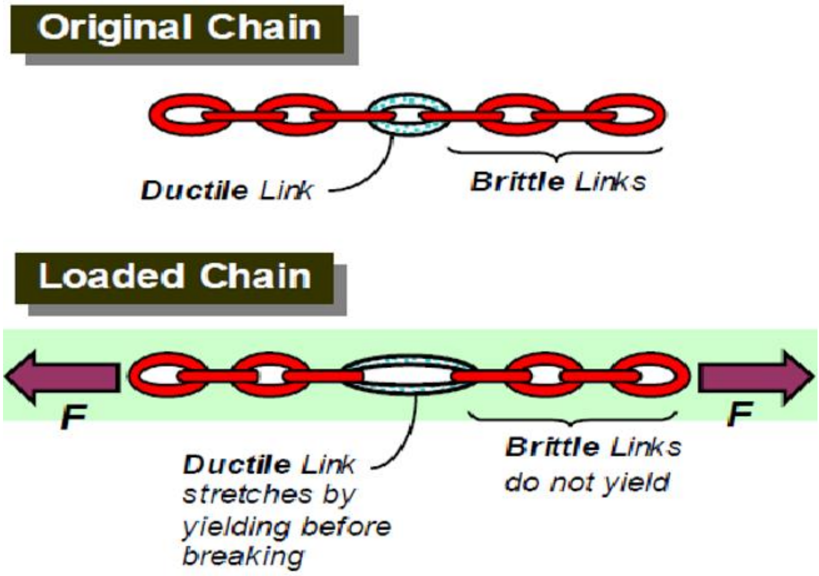

Fig 1.1: Ductile chain design[4]

Soft storey mechanism is considered to be undesirable as the structural response is typically non-ductile (sometimes resulting in collapse) when such a mechanism develops. Several such building failures due to the development of the soft storey mechanism had been observed in past earthquakes. Fig 1.3 shows the failure of a six story building with soft storey ground floor in the 2008 Wenchuan, China earthquake and Fig 1.4 shows a collapse of an open garage apartment building in the 1994 Northridge, LA earthquake.

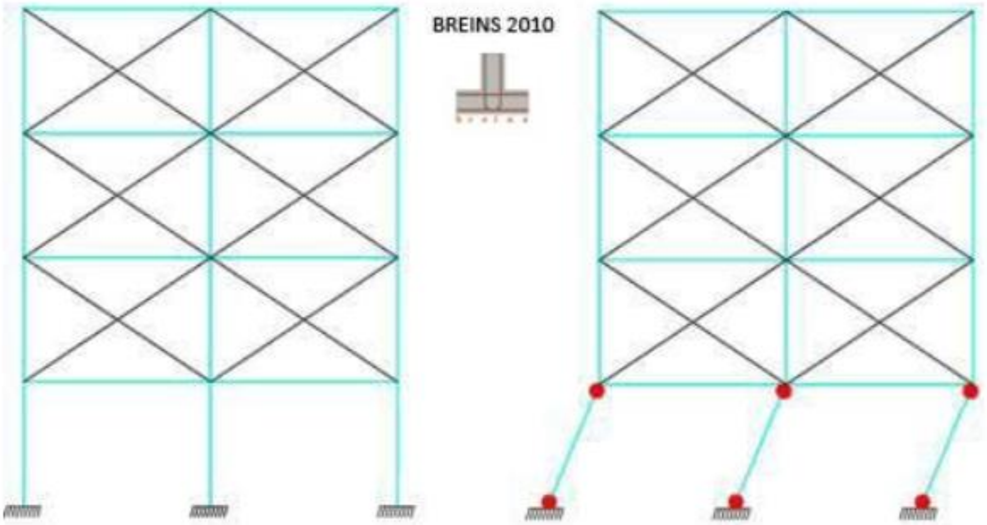

Fig 1.2: A building with soft-storeyed Ground Floor. Model representation of soft storey collapse mechanism

Fig 1.3: A six storeyed building with soft-storeyed ground floor at Dujiangyan in 2008 China earthquake

Fig 1.4: Total collapse of soft storeyed open garage at the ground floor of the apartment building in Northridge earthquake

When trying to design to avoid soft storey mechanism, instead of having hinges formed at the bottom and the top of one storey, we try to form hinges in the beams at their ends. This promotes displacement of the structure to occur over several stories and places less rotational demand on each hinge.

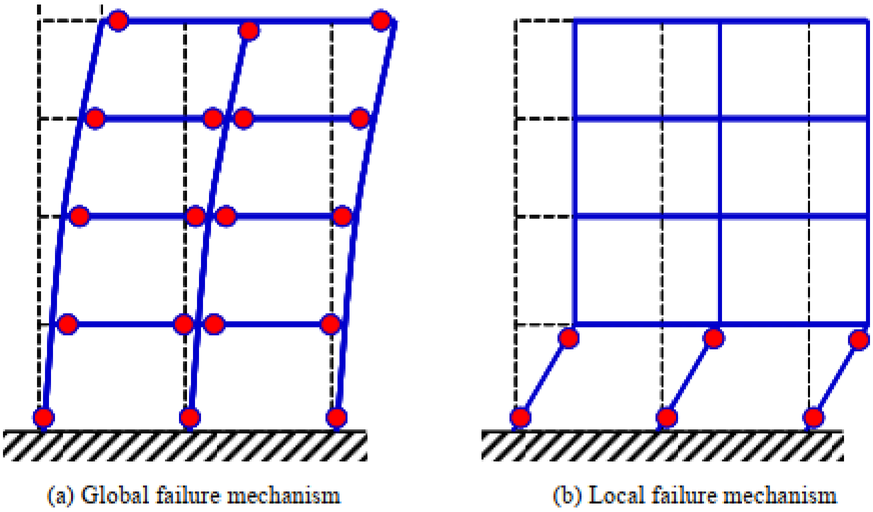

(a) Global failure mechanism

(b) Local failure mechanism

Fig 1.5: Failure mechanisms of structures with "strong column-weak beam" design[5]

As shown in Fig 1.5, when an equal displacement is distributed over several stories, the rotation of the plastic hinges in the so-called "sway mechanism" (Fig 1.5a) as compared to the soft story mechanism (Fig 1.5b). Therefore, when plastic hinges are dispersed over several stories of the frames instead of concentrating on only the first floor column, a much better overall ductility of the system is achieved[5].

In order to accomplish beam sway mechanism and to prevent soft story failure mechanism, hinges need to formed in the beams but not in the columns. In that system, beams need to be sufficiently weaker link than the columns. If the beams are too strong, they won't yield and form hinges.

Special attention was paid to this concept after 1994 Northridge earthquake. Before 1994 Northridge earthquake, engineers believe that steel structures are ductile because structural steels are ductile materials. That turned out not to be the case in the Northridge earthquake. In the earthquake what actually happened was that instead of forming hinges in the beams to initiate the sway mechanism, it was shown that the connections between beams and columns were not ductile enough to allow hinges to form in the beams. After the earthquake, instead of seeing the evidence of yielding of the beams, brittle fractures were found when taking a closer look at the connections between the beams and columns as shown in Fig 1.6. It was discovered that the connections couldn't transfer the forces from the beams to columns, and vice versa. As a result, hinges couldn't be formed in the beam and the building didn't perform in the expected manner, this was a big surprise to structural engineering community.

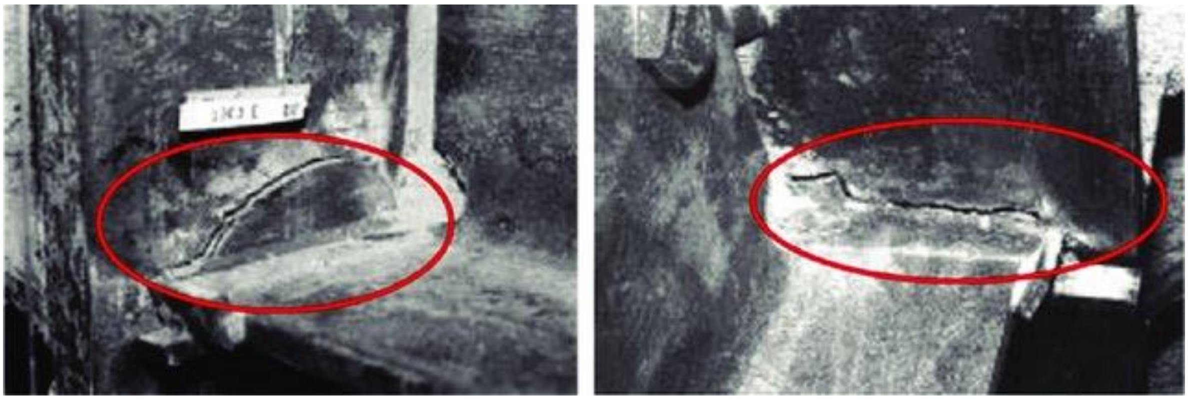

Fig 1.6: Examples of brittle failure of welded beam-column connections during the 1994[6]

The Northridge failures led to investigation and research into all sorts of topics related to this problem. New weld details and weld electrodes which deposit metals with improved toughness were proposed for connections between beams and columns in the high seismic areas. However, research showed these new weld electrodes and weld details alone were not able to provide adequate ductility for the typical welded moment connections. Hence additional overstress mitigation strategies which shift plastic hinging of the beam away from the connection joint were proposed[7], examples of these strategies are shown in Fig 1.7.

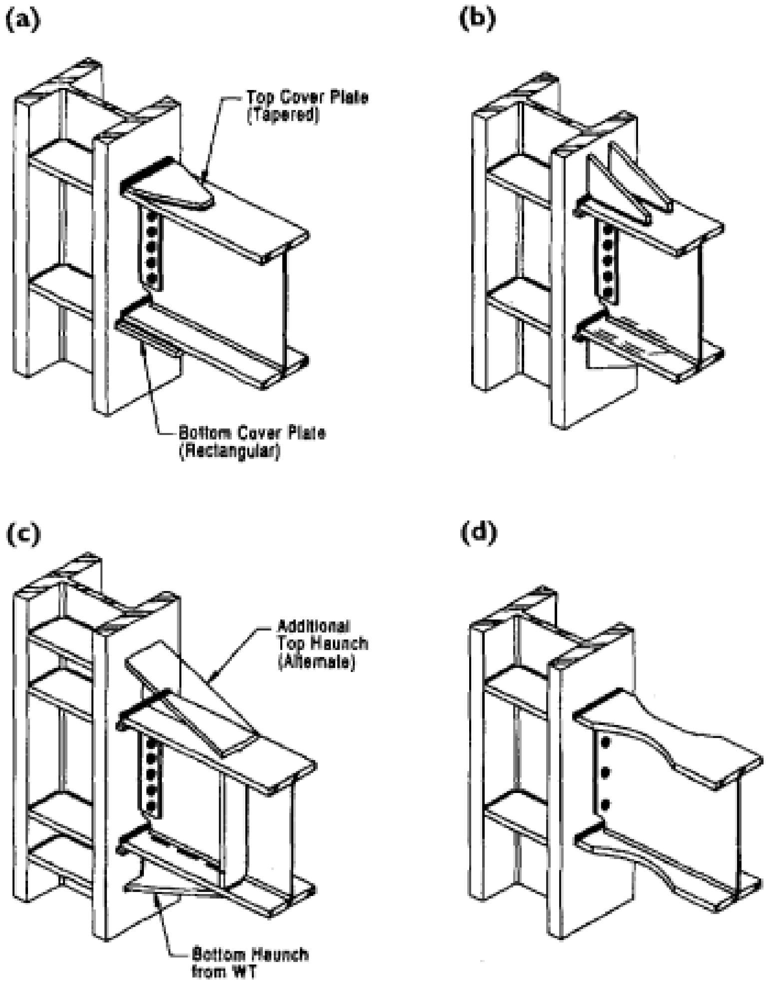

Fig 1.7: Examples of modified moment connection designs: (a) coverplate, (b) upstanding rib, (c) haunch,(d) dogbone[7]

These connections either strengthen and stiffen the connection or weaken the beam away from the connection. In both scenarios yielding and plastic hinging of the beam is promoted away from the connection region. This was found to greatly improve the performance of beam to column connection sub assemblages during laboratory testing. Of the connections shown in Fig 1.7 the reduced beam section (RBS)(Fig 1.7d), also known as the “dogbone” connection is perhaps the most commonly used in practice.

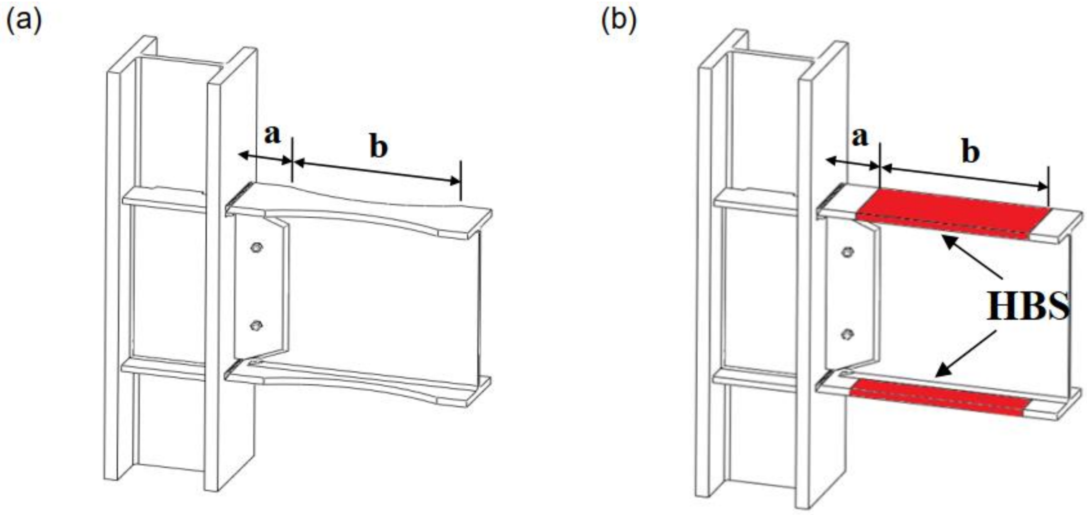

Fig 1.8: Sketch of (a) Reduced Beam Section (RBS) and (b) Heat-treated Beam Section (HBS)[8]

In a RBS connection, part of the beam flanges are selectively cut in the region adjacent to the connection between beam and column. The idea behind RBS is to intentionally make the beam weaker to force plastic hinges to form within the reduced section and to reduce the stresses at the weld. Therefore when a tensile force is applied to the flange, the weakened section will fail before the weld fails.

Intentionally weakening the beams tend not to be a problem for moment frames as their design is governed by the stiffness of the frame and not its strength. With that said, when the beam flanges are cut, the stiffness is reduced, and therefore, deeper beams than otherwise necessary are required. Another disadvantage is that when the flanges are cut, the beams become more susceptible to buckling, and local instability which results in rapid strength loss.

To overcome these disadvantages, an innovative idea was proposed[8, 9], in which the beam flanges are heat treated (Fig 1.8) to get a reduction in the strength of steel in specified areas (see Fig 1.9 for the stress-strain curves showing the strength loss). Note that the beam web can also be heat treated if necessary. Now, because the cross-section area of the beam remains unchanged and the elastic modulus of the heat-treated steel is also unchanged, the stiffness is preserved in this region. The stability of that section is also better than the reduced section.

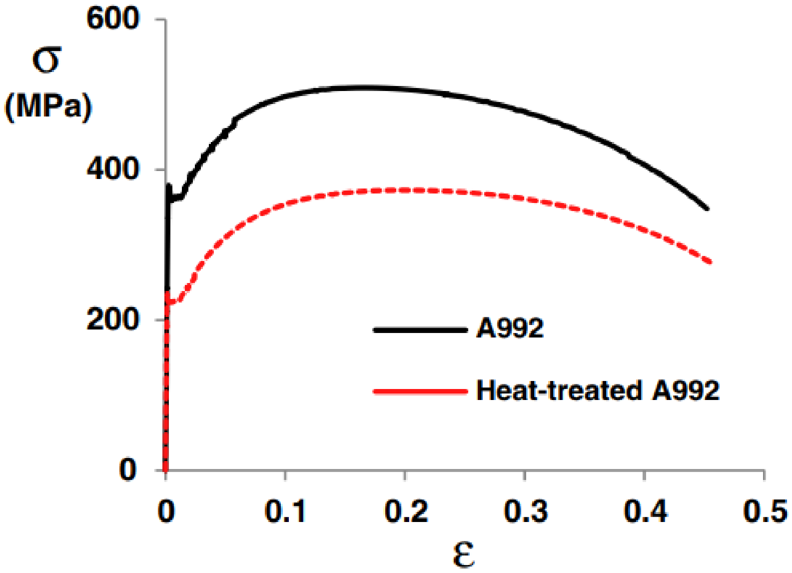

Fig 1.9: Engineering Stress-Strain response of A992 and heat-treated A992 steel[9]

This idea can also be applied to buildings with other types of lateral force resisting systems other than moment resisting frames. The big advantage of this approach is that it doesn’t affect the elastic stiffness of the structure, it reduces seismic forces on the structure, and it provides protection against unwanted connection failures.

Another common lateral load resisting system in steel buildings are braced frames. Two types of braced frames are shown in Fig 1.10 namely eccentric (Fig 1.10a) and concentrically braced frames (Fig 1.10b)[10].

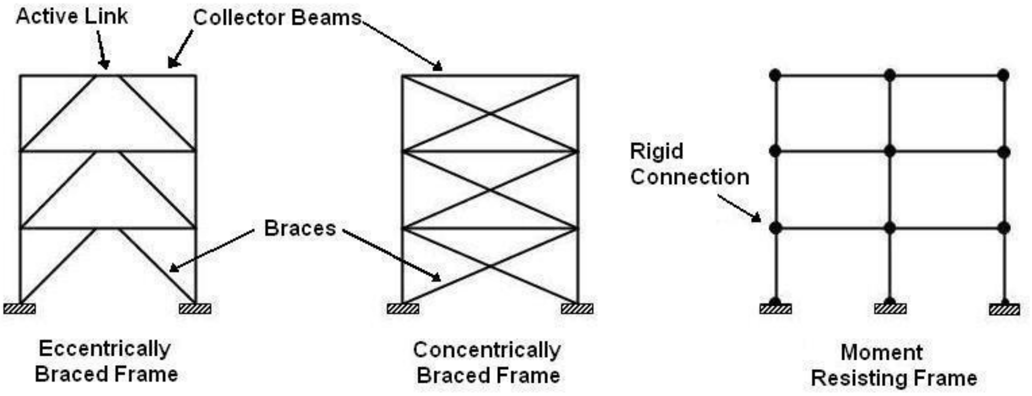

Fig 1.10: Structural steel seismic load resisting systems[10]

Brace frames have high lateral stiffness and are therefore more economical than moment resisting frames. This stiffness is achieved by the truss action which is provided by diagonal braces. In concentrically braced frames the braces are the deformation-controlled elements and the beams and columns the force-controlled elements. The braces are often constructed from rectangular hollow sections which are made by cold forming steel sheets to form the section shown in Fig 1.11. As a result of this cold forming the strength of steel increases significantly and this causes the braces to have significantly higher strength than is needed for seismic design. As a consequence of this strengthening, the columns, beams, connections and even the foundations have to be made stronger to satisfy capacity design principles. In addition, the strengthening of the braces tends to reduce their ductility. Hence heat treating the braces in concentrically braced frames has the potential to reduce overstrength and improve ductility.

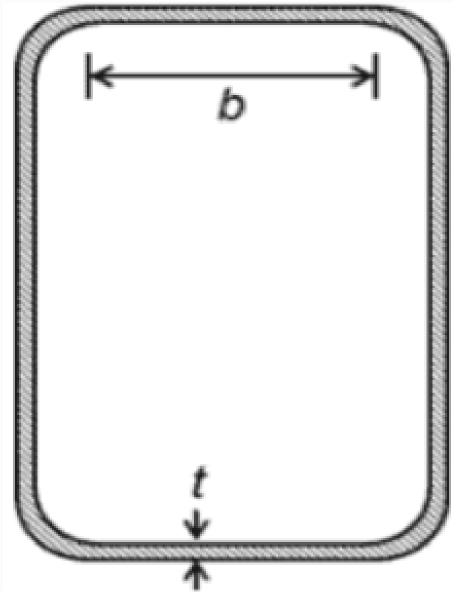

Fig 1.11: Diagram of the width and thickness dimensions used to calculate width-thickness ration (b/t)

The motivation behind the study presented herein is to develop a frame work in which heat treatment parameters to achieve target material properties can be specified given the chemical composition, and initial microstructure of the steel. The goal is to provide recommendations for heat-treating steels for future applications of this concept.

This goal is achieved through metallurgical studies, mechanical testing and by taking advantage of strength-property relationships for low carbon steels.

Chapter 2

Material and methods

In this study only ASTM A992 steel, considered as the most commonly used structural steel for wide flange beams in the USA, is used.

Tremendous changes in the manufacturing process of rolled structural steel shapes have taken place by the end of last century. The changes include the transition from ingot-casting to continuous casting in practically every steel mill in the world as well as the switch from iron ore based production to the main use of recycled material in most mills.

These changes have greatly lowered production costs and improved mill efficiency in the steel industry, while at the same time a slightly different chemical composition was introduced to the steel. Metallic impurities and alloying elements are more abundant in modern steels than in traditional ones because of the use of scrap automobiles and large appliances in the recycling process. To some extent, theses metals affect the materials strength and properties. The ASTM standard didn’t put limits on the amount of these elements for A36 and A 572 Grade 50 steels[11, 12].

ASTM A992 is the preferred material specification for wide-flange shapes which has replaced ASTM A36 and A572 Grade 50. The major advantage of A992 is its better material definition.

These steels have restrictions on the maximum carbon equivalents that depend on the grade and weight of the produced steel. With a maximum permissible carbon equivalent value of 0.47% for shapes with flange thickness over 2 in. [50 mm] and 0.45 % in other shapes required, weldability of the steel is improved. The carbon equivalent shall be calculated using the following formula:

$$CE = C + (Mn)/6 + (Cr + Mo + V)/5 + (Ni + Cu)/15 \tag{2.1}$$

In addition to the restrictions on the maximum carbon equivalent in A992 steels, additional consideration is given to the maximum yield strength and yield strength to tensile strength ratio. Material ductility is well defined in A992 steels. Ductile behavior is vital in seismic design in which the structure need to accommodate accidental overloads. In an earthquake, plastic hinges need to be designed to form in beams and undergo high level of cyclic plastic rotation in order to accommodate displacements as well as dissipate seismic energy. The ratio of yield strength to ultimate tensile strength essentially describes the amount of post-yield load the material can handle before fracture. The lower the ratio is, the more energy the hinge can absorb during an earthquake. The ASTM A992 specification specifies a maximum yield strength to tensile strength ratio as 0.85. As a comparison, the nominal value for A572 Grade 50 steel is 50 ksi/65 ksi=0.77[11, 12].

The chemical composition of A992 steels shall conform to the requirements in Table 2.1. The material as represented by the test specimens shall conform to the requirements for tensile properties prescribed in Table 2.2.

Table 2.1: Chemical requirements of A992 steels (Heat analysis)[13]

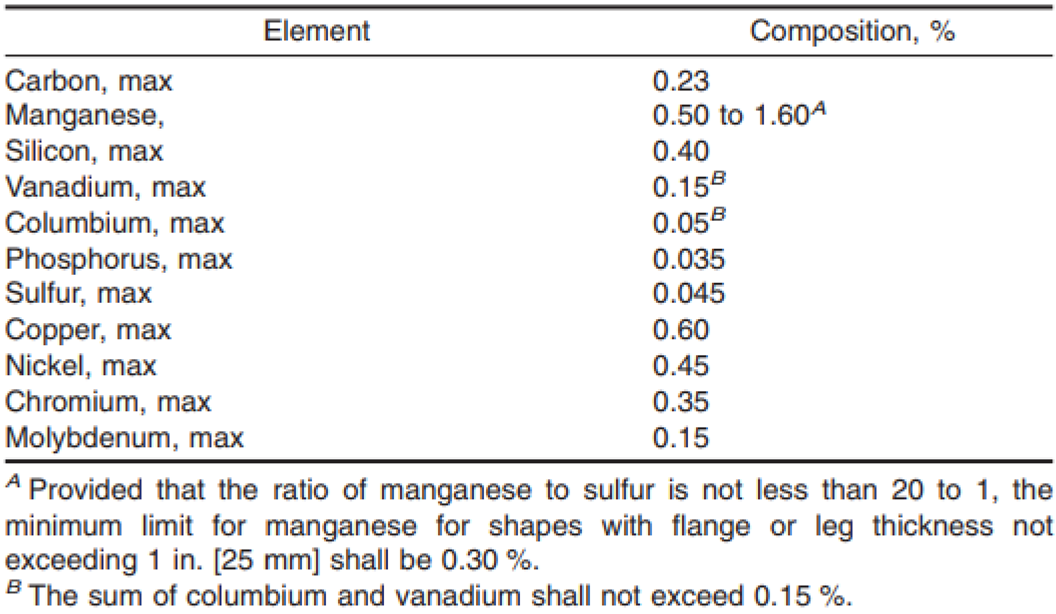

Element	Composition, %
Carbon, max	0.23
Manganese,	0.50 to 1.60[A]
Silicon, max	0.40
Vanadium, max	0.15[B]
Columbium, max	0.05[B]
Phosphorus, max	0.035
Sulfur, max	0.045
Copper, max	0.60
Nickel, max	0.45
Chromium, max	0.35
Molybdenum, max	0.15

[A] Provided that the ratio of manganese to sulfur is not less than 20 to 1, the minimum limit for manganese for shapes with flange or leg thickness not exceeding 1 in. [25 mm] shall be 0.30 %.

[B] The sum of columbium and vanadium shall not exceed 0.15 %.

Table 2.2: Tensile requirements of A992 steels[13]

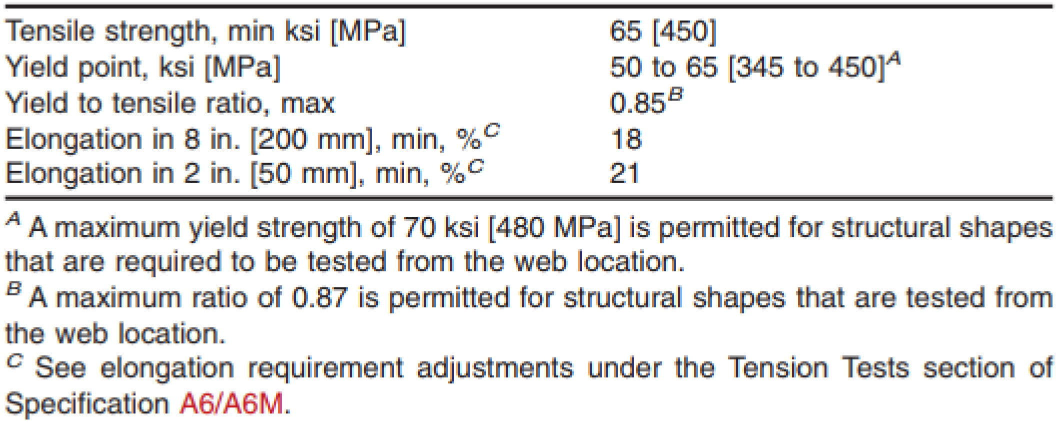

Tensile strength, min ksi [MPa]	65 [450]
Yield point, ksi [MPa]	50 to 65 [345 to 450][A]
Yield to tensile ratio, max	0.85[B]
Elongation in 8 in. [200 mm], min, %[C]	18
Elongation in 2 in. [50 mm], min, %[C]	21

[A] A maximum yield strength of 70 ksi [480 MPa] is permitted for structural shapes that are required to be tested from the web location.

[B] A maximum ratio of 0.87 is permitted for structural shapes that are tested from the web location.

[C] See elongation requirement adjustments under the Tension Tests section of Specification A6/A6M.

2.1 Materials selection

A typical ASTM A992 steel was selected to be the reference material of this investigation since it is one of the most commonly used structural steels at present.

Six steel blocks with different chemical compositions were cut from the flanges of wide flange steel members and were picked to study the effect of chemical composition on austenite grain growth, ferrite grain growth and final mechanical properties. The chemical compositions of these 6 steels are listed in Table 2.3.

Table 2.3 : Chemical compositions of studied steels

Sample	Elements(wt%)												
	C	Mn	P	S	Si	Cu	Ni	Cr	Mo	V	Nb	Sn	N
1	0.07	1.12	0.011	0.022	0.22	0.29	0.09	0.11	0.02	0	0.019	0.01	NA
2	0.08	1.31	0.016	0.021	0.26	0.27	0.16	0.14	0.04	0.04	0.001	0.01	NA
3	0.08	1	0.01	0.024	0.2	0.32	0.13	0.1	0.04	0.01	0.02	0.01	NA
4	0.17	1.02	0.022	0.011	0.14	0.24	0.08	0.13	0.02	0.032	0.002	0.011	NA
6	0.15	1.1	0.012	0.006	0.19	0.22	0.07	0.09	0.02	0.012	0.01	0.017	0.012
8	0.26	1.16	0.014	0.011	0.22	0.23	0.08	0.09	0.019	0.038	0.002	0.01	0.009

2.2 Experimental approach

The experimental study was aimed at firstly understanding the effect of heat treatment on the microstructure of A992 steels with different chemical compositions and using structure property relationships to predict steel yield strength based on the microstructure. Low carbon steels undergo a solid-state phase transformation which is of primary significance for heat treating. Therefore, the study starts with understanding the effect of heat treating on the austenite phase which then leads to the study of the effects on the ferrite phase. These microstructural studies were carried out by heat treating steels and then performing traditional metallographic studies to analyze their microstructure. Once the microstructural effects were analyzed, mechanical testing was carried out and then structure-property relationships were applied to the experimental data.

2.2.1 Heat treatments

2.2.1.1 Austenite grain coarsening studies

To study the grain coarsening of austenite, different heat treatments were applied to steel samples of A992 cut from steel blocks mentioned earlier. Six samples with different chemical compositions were selected.

Samples of 25*25*25mm (1 cubic inch) were heated up to different temperatures ranging from 900 to 1200°C at increments of 150°C in a ST-1500C-121216 High Temperature Box Furnace, as shown in Fig 2.1. The samples were then held at peak temperature for different time of 10, 100 and 1000 minutes respectively. Then the samples were water quenched in water buckets to retain the austenite grain sizes formed at different heating conditions. All samples were heated up to the peak temperature with heating rate of 10°C/min.

Fig 2.1: ST-1500C-121216 High Temperature Box Furnace

Following the heat treatments, samples were cut, mounted, grinded and polished before etching to reveal grain boundaries. Samples were prepared for microstructural analysis using optical microscope to determine austenite grain sizes from each heat treatment. Based on the results of preliminary heat treating trials, additional further heat treatments were done for selected samples.

2.2.1.2 Ferrite grain growth study

The material used in the ferrite study was selected from Table 2.3. To study the effect of chemical composition on ferrite grain growth, samples 2, 3, and 4 were used based on previous study of austenite grain growth. Different heat treatments were applied to steel samples.

Samples of 25*25*25mm (1 cubic inch) were austenitized at 900, 1050 or 1200°C for 100 min and cooled at various rates at 0.1, 1 or 5°C/min down to 500°C to transform them into ferrite. Samples were held at 500°C for 30 minutes to reach thermal equilibrium and then air cooled.

It is worth noting that especially for the slow cooling rates, different heat treatments were used for time consideration. After samples were held at austenitizing temperature for 100 minutes, they were cooled at 6°C/min down to a temperature (Tx) at which they were held for 100 minutes before subjecting to various cooling rates. This temperature must be somewhere above Ar3 temperature to assure that no phase transformation takes place from austenitizing temperature to Tx. Tx was set as 900°C based on Ar3 temperature which was predicted using empirical equations. This heat treatment process is illustrated by Fig 2.2.

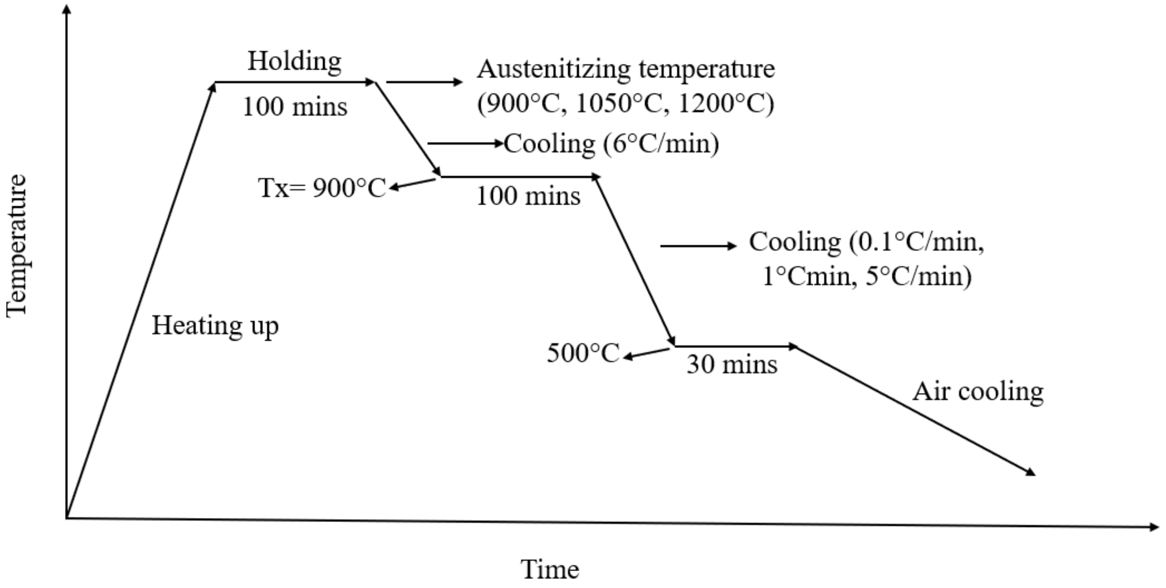

Fig 2.2: Heat treatment for ferrite grain growth study

2.2.2 Microstructural analysis

2.2.2.1 Optical Microscopy

Optical metallography samples in this study were prepared using standard techniques by progressively grinding on 120, 220, 600, 1200 grit silicon carbide grinding pads. The grinding steps gradually increase in the time and reduce in pressure applied to the sample as the steps progress from coarse to fine papers. The samples were then polished with 1 micron and 3 micron diamond suspension. Different etching procedures were used due to either prior austenite or ferrite-pearlite structures.

The ferrite-pearlite microstructure of the original non heat-treated samples and the heat treated samples using a 5% nital etching solution(95 ml ethanol and 5 ml nitric acid) at room temperature for 10-20 seconds.

Compared to ferrite-pearlite microstructures, the etching for revealing prior austenite grain boundaries of as-quenched samples was much more difficult. Considering the difficulty of revealing prior austenite grain boundaries, another 12 hours of tempering at 490℃ was applied to the samples following the normal heat treatment process. This tempering process allows phosphorus in solution to segregate towards the prior austenite grain boundaries and aid the optical metallographic techniques by revealing sharp and clear austenite grain boundaries when etching with picric acid[14]. The prior austenite grain boundaries were then revealed by a special etching solution which consists of 5g of picric acid, 100 ml of distilled water and a wetting agent, which was 4g of dodecylbenzene sodium (SDBS) in our study. In addition, 1 ml of HCl (hydrochloric acid) was also added to the etchant to make it more aggressive. The etchant was heated to 80-90°C, and the samples were immersed in the solution for 15-90 seconds depending on different their chemical composition and different heat treatments they underwent. Lightly re-polishing by hand on a stationary 1 micron diamond suspension polishing cloth was used to remove some of the unimportant background details, making it easier to see grain boundaries . Samples were finally cleaned up with methanal and dried with compressed air before inspecting with optical microscope.

Although lots of efforts were paid to etching with picric acid, it still failed to reveal prior austenite grain boundaries in some samples, especially those heat treated at the highest temperature. In order to reveal the austenite grain structure of those samples, a different technique which outlines the prior austenite grains with small ferrite grains that nucleate on austenite grain boundaries was used. Instead of heating the samples up to a peak temperature, holding for a certain period of time and then water quenching, a complete different heat treatment process was applied. After held at the peak temperature for some time, those samples were cooled down to 800°C at 15°C/min cooling rate and then at 5°C/min to 715°C then water quenched at different temperatures. With this heat treatment process, since the samples were cooled down below Ar3 temperature, ferrite allotriomorphs nucleated at the austenite boundaries and decorated them so that the prior austenite grains could be revealed. For these samples, Nital etchant (95 ml ethanol and 5 ml nitric acid) were used to reveal the ferrite grains at the prior austenite grain boundaries. Comparison between the results of two etching technique is discussed later.

The austenite and ferrite grain sizes were measured by ImageJ image processing program. The standard intercept test method was applied to determine average austenite and ferrite grain size. The systematic manual point count test method, as well as ImageJ, was used for statistically estimating the volume fraction of ferrite/pearlite of samples which were heat treated differently.

2.2.2.2 Scanning Electron Microscopy

Electron Backscatter Diffraction (EBSD) and energy dispersive x-ray (EDS) spectroscopy were used for the characterization of grain size distribution and chemical compositions.

FEI Apreo Field Emission Scanning Electron Microscope (FE-SEM) equipped with symmetry detector from Oxford Instruments were employed for EBSD analysis. The AZtec software was used to acquire the EBSD data under different experimental conditions. After the test, the microstructure was analyzed by Tango, Project Manager Channel 5 software. The working distance of the microscope was 15-20 mm, and the microscope worked under a beam current of 26 nA and accelerating voltage of 20.00 kV. The spacing between adjacent EBSD measuring points, which is defined as step size, was set as either 2.5 or 5 microns depending on different ferrite grain sizes. An appropriate step size was selected such that it neither leads to a very long mapping time nor misses information of unusually small grains. A magnification of 50X or 100X was used to assure that the number of grains is enough to get an overall grain size distribution.

Samples for EBSD analysis were prepared using the same technique used for optical microscopy analysis plus 2 steps of polishing. The normal diamond polishing steps were followed with low pressure oxide polishing for 25 minutes to make the surface free from deformation. Samples were then polished with DI water to remove polishing media.

2.2.3 Mechanical properties

2.2.3.1 Vickers Hardness and dislocation density

Microhardness measurements of all samples were carried out using LECO Microhardness Tester. Test samples were indented with a diamond indenter, in the form of a right pyramid with a square base and an angle of 136 degrees between opposite faces. Indentation load was chosen as 1000 grams during the test. The full load was applied for 15 seconds on all samples. The horizontal indent length and vertical indent length were measured with an optical microscope, based on which the arithmetic mean of the two diagonals was calculated.

The Vickers hardness number, in terms of grams-force and micrometers, is calculated as follows[15]:

$$HV = 1000\ X\ 1.8544\ X\ \frac{F(gf)}{d_V^2(um)} = 1854.4\ X\ \frac{F(gf)}{d_V^2(um)}\ , \qquad (2.2)$$

For each sample, the average hardness was calculated from at least 20 indentations for statistical validity.

Moreover, microhardness measurements were conducted at different loads of 25 gf, 50 gf, and 1000 gf in order to determine the dislocation density of all samples. The increase of measured hardness values with the decrease of indentation depth is explained by the indentation size effect (ISE). According to Nix and Gao[16], the ISE results from an increase in the density of the geometrically necessary dislocations required to accommodate the plastic deformation gradient around the indentation. A model was developed to deduce a simple expression which relates hardness with indentation depth:

$$\left(\frac{H}{H_0}\right)^2 = 1 + h^* \cdot \left(\frac{1}{h}\right) \tag{2.3}$$

Where H_0 in the limitation of infinite depth (bulk hardness, which was obtained using a 1000 gf force in this study), h^* is a characteristic length, and H is the hardness value corresponding to indentation depth h.

By fitting Eq. to the experimental hardness values (see the regression curve in Fig 3.31), a value of h^* could be obtained. The Nix and Gao model enables relating this parameter to the dislocation density by:

$$\rho = \frac{3}{2}\frac{1}{f^3}\frac{tan^2\theta}{bh^*}, \tag{2.4}$$

where ρ is the density of dislocations statistically stored in the lattice, θ is the angle between the surface of the material and the surface of the indenter, b is the Burgers vector of the dislocations and f is a correction factor for the size of the plastic zone. In this work θ = 22°, f = 1.9, and b = 0.25 nm. By introducing these values into Equation 2.3, ρ was approximately estimated[17, 18].

2.2.3.2 Rockwell Hardness

The Rockwell indenter uses two loads to determine the hardness. The minor load is applied to establish the zero point. This is typically done to get beyond surface scales and debris that may otherwise influence the measurement. Sometimes it is necessary to ensure that the sample surface is relatively clean from oxide and scale buildup prior to the test by employing a very light grinding or wet sanding technique.

After the application of the minor load, the major load is then applied for a short period of time, causing further indentation beyond the application of the minor load. After a period of time, the major load is released while the minor load is still applied. The difference in the indentation depths between the major and minor loads represents the hardness.

In the present work, all samples with ferrite-pearlite microstructure were measured on Rockwell Hardness B scale using a 1/16 inch diameter carbide ball indenter. Minor load was 10 kgf and major load was 100 kgf. The dwell time was set as 2.0 seconds in Rockwell hardness testing.

The average value of Rockwell hardness was calculated from at least five indentations for each sample. After following the procedure for a fully manual hardness tester, Rockwell hardness measurements were carried out using an automated hardness tester.

2.2.3.3 Tensile test

In this work, tensile tests were carried out in accordance with ASTM A370 for the purpose of determining yield strength, tensile strength, uniform elongation and total elongation to investigate the effect of heat treatments on tensile properties.

Test coupons were obtained by machining heat treated steel slabs. The cross section of the test pieces are rectangular. The original cross-section area was calculated from measurements of the dimensions of the tensile bar. The test pieces are shown in Fig 2.3.

In order to measure the total elongation, two gauge marks two inches apart on the center axis of the coupon were made using a puncher. After fracture, two broken pieces were carefully fitted back together so that their axes lie in a straight line. Special precaution was taken to ensure proper contact between the broken parts. By measuring the distance between two punch marks again after fracture, the total elongation was calculated.

All tensile specimens were tested in Instron Load Frame. An extensometer of 25.4 mm gage length was used for accurate measurement of strain. Two different loading rate were applied during the rest: 1.5 mm/min before 5% strain and 10 mm/min after. The extensometer was removed after the maximum force in the test was reached to protect it from damage during fracture.

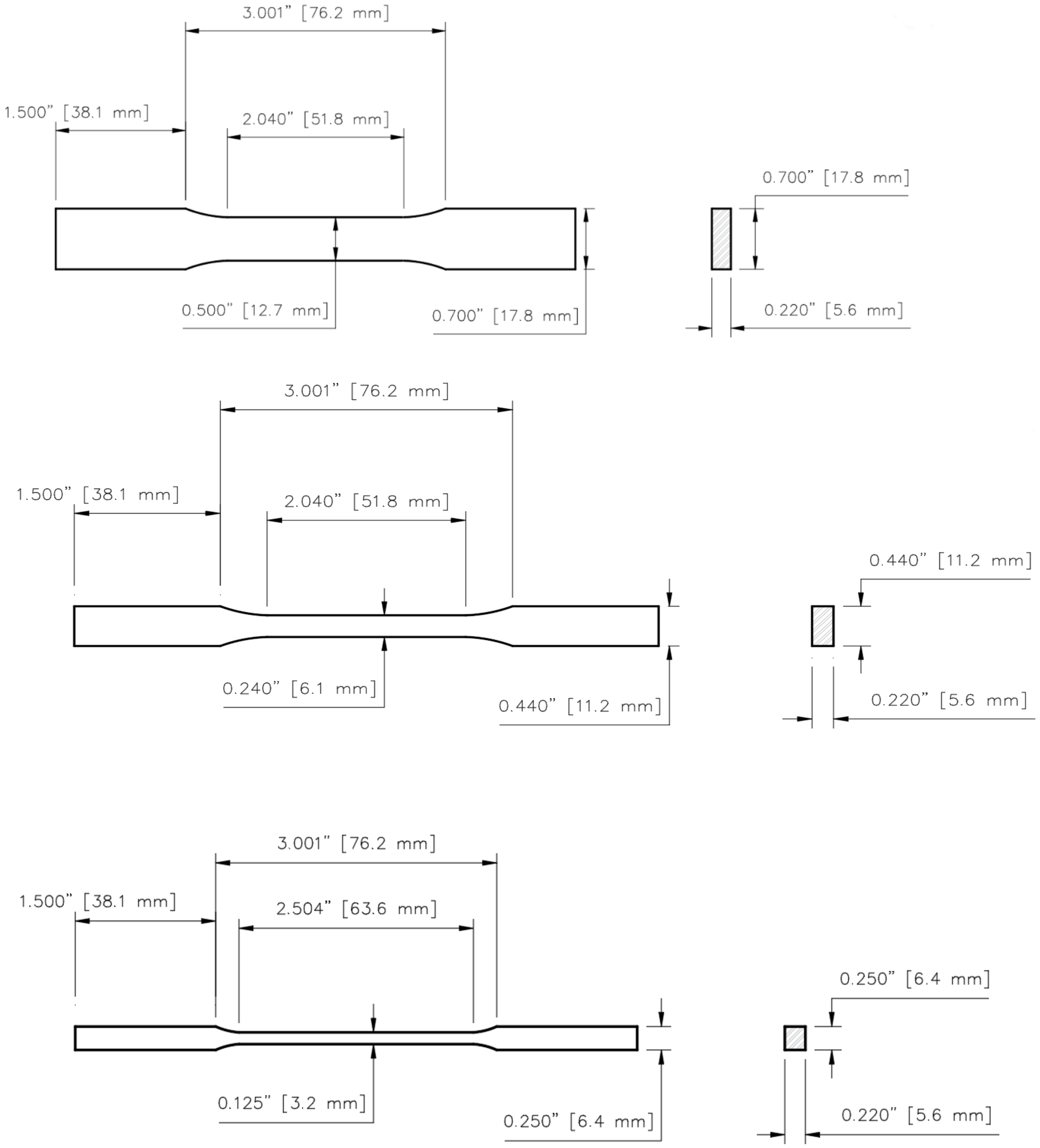

Fig 2.3: Sketch of tensile coupons

Chapter 3

Results and discussion

The microstructural features and mechanical properties are discussed in the following section.

3.1 Original microstructures

The microstructure of non-heat treated samples is shown in Fig 3.1. The grain sizes and phase volume fractions of exhibited samples are reported in Table 3.1. Under the optical microscope, the light areas represent the ferrite phase and the dark areas represent the pearlite colonies. As shown in Fig 3.1, all three A992 steels with different chemical compositions have ferrite-pearlite microstructures, while the grain size and volume fractions of ferrite and pearlite vary. Sample 3 and sample 4 have similar ferrite grain sizes of 9.69 μm and 9.96 μm, while the ferrite grain size of sample 2 is 5.9 μm, which is much smaller compared to sample 3 and 4. Sample 2 and 3 both have a pearlite volume fraction around 11%, while the pearlite volume fraction of sample 4 is about 30%. The difference in ferrite grain size and pearlite volume fraction can be attributed to the different chemical compositions of these steels. Manganese content of sample 2 is 1.31%, which is higher than that of sample 3 (1%) and sample 4 (1.02%). Mn lowers the $\gamma \rightarrow \alpha$ (austenite to ferrite) transformation start temperature, which leads to the increase in nucleation rate of ferrite and the decrease in ferrite growth rate. As a result, ferrite grain refinement is achieved. The carbon content of sample 4 is 0.17%, which almost twice that of sample 2 and 3 (0.08%). Therefore, the volume fraction of pearlite in sample 4 is much higher.

Table 3.1: Microstructural properties of three non-heat treated steels

Sample	Ferrite Grain Size(um)	Pearlite Volume Fraction(%)	Ferrite Volume Fraction(%)
2	5.9	11.6	88.4
3	9.69	10.98	89.02
4	9.96	29.49	70.51

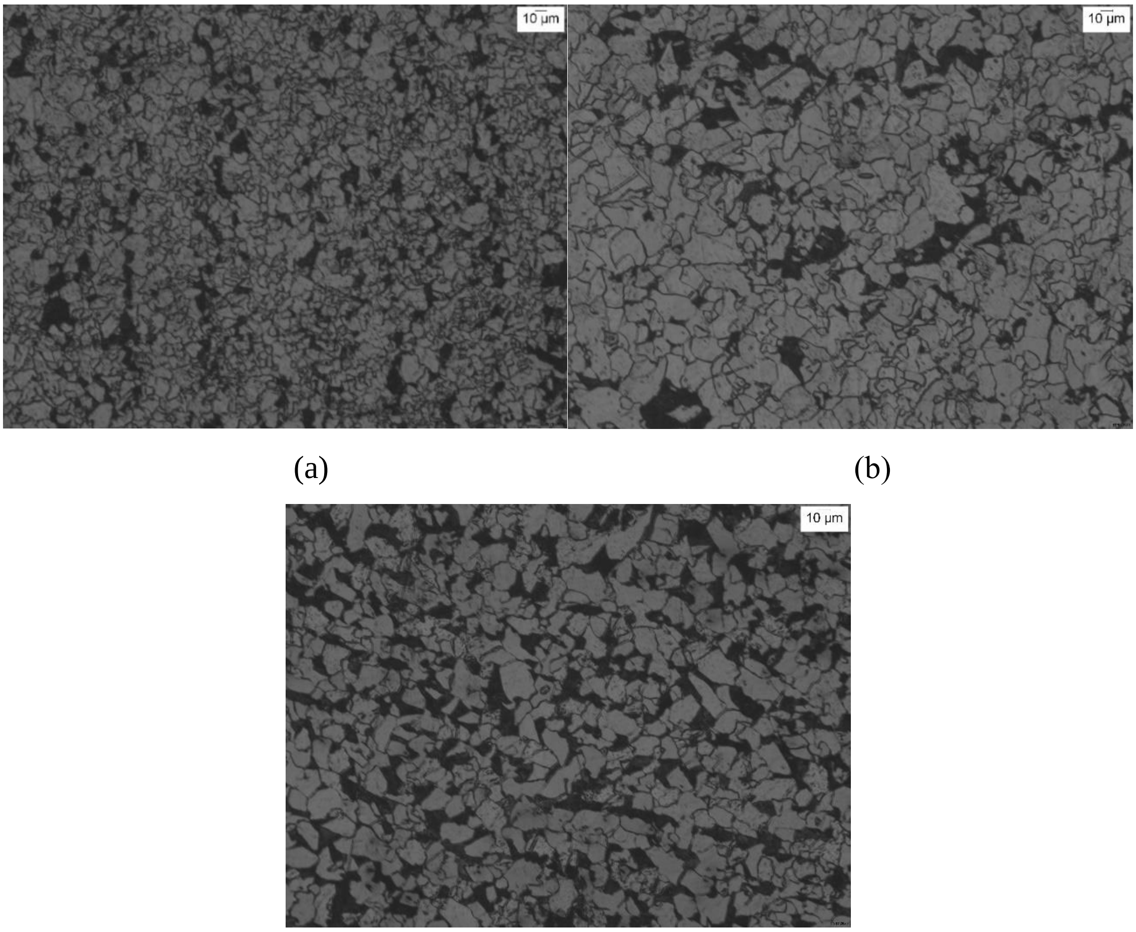

(a) (b)

(c)

Fig 3.1: Optical micrographs showing the microstructures of non-heated samples at 200X magnification: (a) Sample 2, (b) sample 3, (c)sample 4.

3.2 Austenite grain coarsening behavior

Considering the difficulty of etching of martensite grains, a different technique which outlines the grains with ferrite was also used to reveal prior austenite grain boundaries. The comparison between two heat treatment and etching technique is shown in Fig 3.3. As shown in Fig 3.3(a), for sample 4 (austenitized at 900°C and held for 100 mins), the prior austenite grain boundaries are successfully revealed using picral etchant. In Fig 3.3(b), the prior austenite grain boundaries are also outlined by the ferrite allotriomorphs that precipitate at the grain boundaries. To avoid the overgrowth of ferrite which will mask the prior austenite grain size, the cooling rate from prior austenite region was strictly controlled to allow only a small amount of ferrite to precipitate. By using the linear intercept method, the average austenite grain size was determined as (a) 11.03 μm and (b) 13.46 μm, respectively. Hence it shows that two technique give similar austenite grain sizes. Two technique were both used in the following study of austenite grain coarsening behavior.

Fig 3.4–Fig 3.13 shows prior austenite grains of sample 2, 3, and 4 after subjected to various austenitizing temperature and holding time. The austenite grain sizes are quantitatively represented in Table 3.2-Table 3.4. The effect of temperature and holding time on the austenite grain size are shown in Fig 3.14 and Fig 3.15, respectively. The images and measured austenite grain size values indicate that the prior austenite grain size increases with higher temperature. Higher temperature drives grains to grow faster to larger dimensions. However, holding time doesn’t appear to have a significant effect on austenite grain size. This can be explained that austenite grain growth has almost stopped after the samples were held for more than 10 minutes.

What’s more, austenite starts to form and grow at phase transformation temperature (Ac3), which is actually much lower than the peak temperature (900°C, 1050°C and 1200°C), so in the study austenite grains have grew for longer time than expected. It can be inferred that at the very beginning, the austenite grains become larger as samples being held for longer time, while the growth speed becomes slower over time. In the study austenite grains have almost stopped growing before quenching at the peak temperature.

In order to establish a reliable quantitative method of predicting austenite grain growth, more heat treatments were applied to sample 3 and 4 at temperatures ranging from 975°C to 1275°C with an increment of 150°C. Since the holding time in real industrial process is typically longer than 10 minutes, austenite grain coarsening behavior with very short holding time wasn’t studied here. Holding time was selected as 100 minutes in these supplementary experiments.

Fig 3.14 illustrates that austenite grains grow linearly with increasing heating temperature for both sample 3 and sample 4. The austenite grain growth rate of sample 4 is constant with respect to temperature in temperature range from 900°C to 1275°C, while for sample 3, there is a turning point at 1050°C where the austenite grain growth rate increases rapidly.

This difference on austenite grain growth rate can be explained by microalloying elements. For sample 3, at a temperature lower than 1050°C, the coarsening of austenite grains during heating is restricted by the niobium carbides. The austenite grain boundaries are pinned by the niobium carbides as they remain undissolved in the austenite phase during austenitization. Above 1050°C, with the increase of the temperature, the niobium carbides dissolve and the pinning effect becomes smaller, resulting in an increase in the austenite grain growth rate.

The consistent austenite grain growth rate of sample 4 can be attributed to the different behavior of vanadium carbides. According to Fig 3.2, the solubility of vanadium carbides are much higher than those of the other alloying element carbides/nitrides at the same temperature, so the austenite grain boundaries are not effectively pinned by the vanadium carbides.. Therefore, there is no change of austenite grain growth rate in vanadium microalloyed steels.

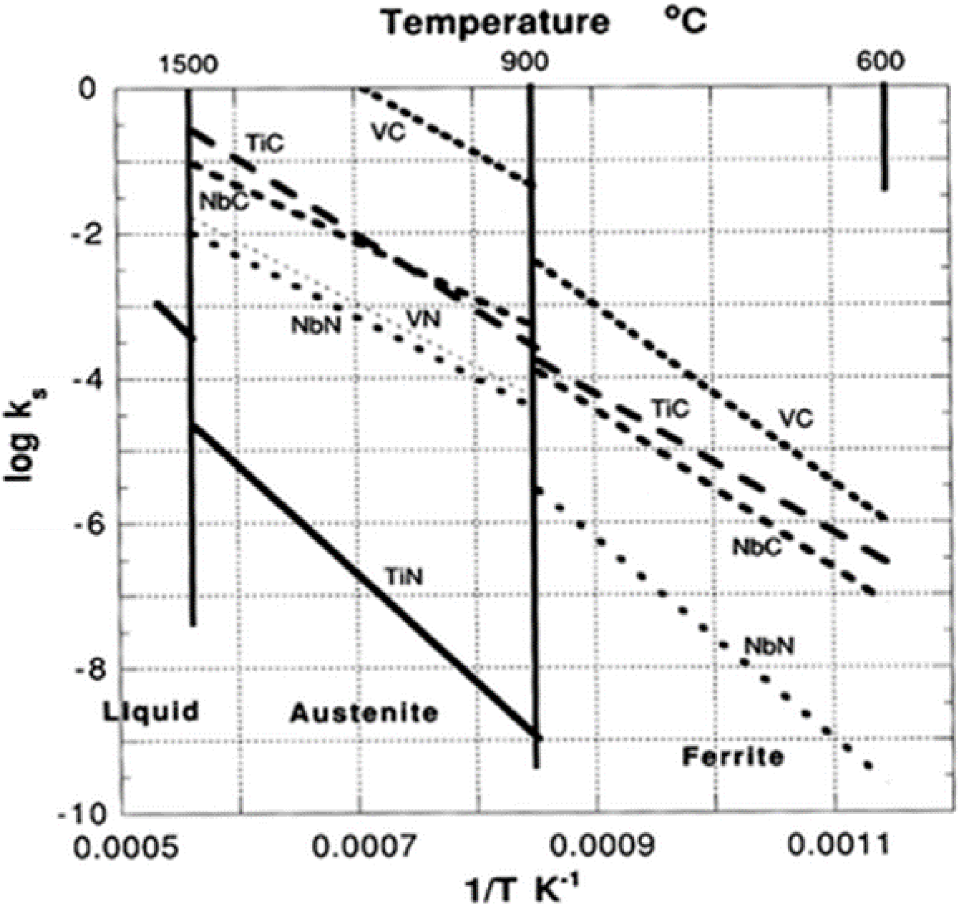

Fig 3.2: Equilibrium solubility products for microalloyed carbides and nitrides in austenite and ferrite[19]

Linear regression equations are proposed to predict the austenite grain growth at various temperatures.

The calibrated equations are as follows:

Sample 4 (Vanadium Microalloyed steel):

$$D_\gamma = 0.4686T - 407.36 \tag{3.1}$$

Sample 3 (Niobium Microalloyed steel):

$$900\text{-}1050°C: D_\gamma = 0.1688T - 135.73 \tag{3.2}$$

$$1050\text{-}1275°C: D_\gamma = 0.8444T - 853.29 \tag{3.3}$$

where D_γ = austenite grain size (um); and T = temperature (°C)

The austenite grain sizes obtained from the linear regression analysis is able to predict the austenite grain growth of sample 3 and sample 4 with reasonable accuracy in the full temperature range (900-1275°C). Other than the effect of Niobium and Vanadium, effects of other elements (e.g. Carbon) on austenite grain growth are not observed.

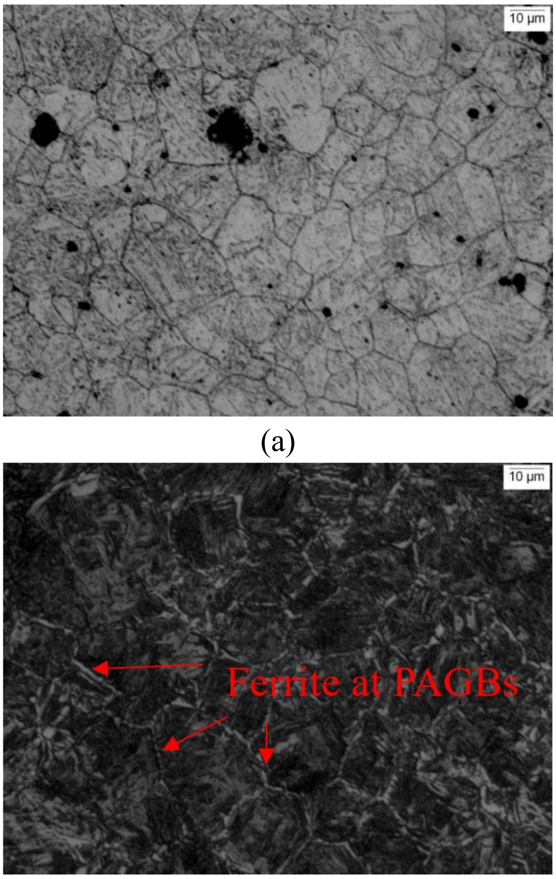

(a)

(b)

Fig 3.3: Prior austenite grains of Sample 4 (austenitized at 900°C and held for 100 mins) revealed by two different techniques, 100X magnification: (a) PAGBS revealed by picral etchant, (b) PAGBs revealed by ferrite growing on the boundaries using nital etchant

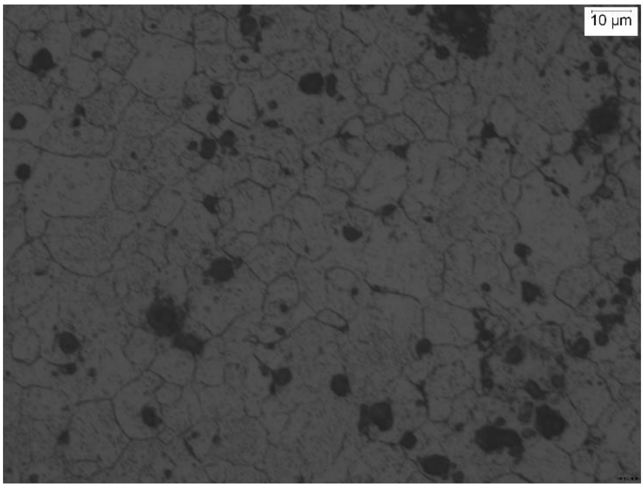

900°C, 10 mins, 500x

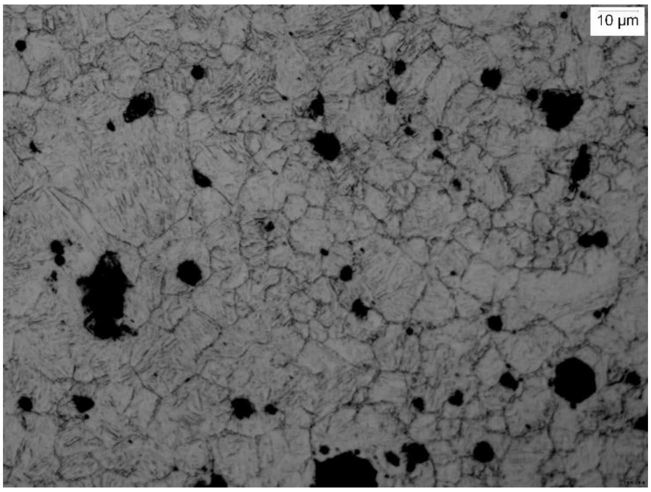

900°C, 100 mins, 500x

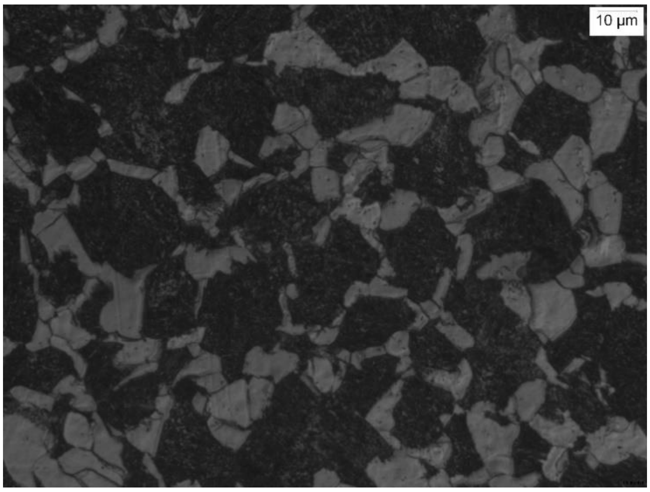

900°C, 1000 mins, 500x

Fig 3.4: Micrograph of prior austenite grains of sample 2 after austenitizing at 900°C and water quenching

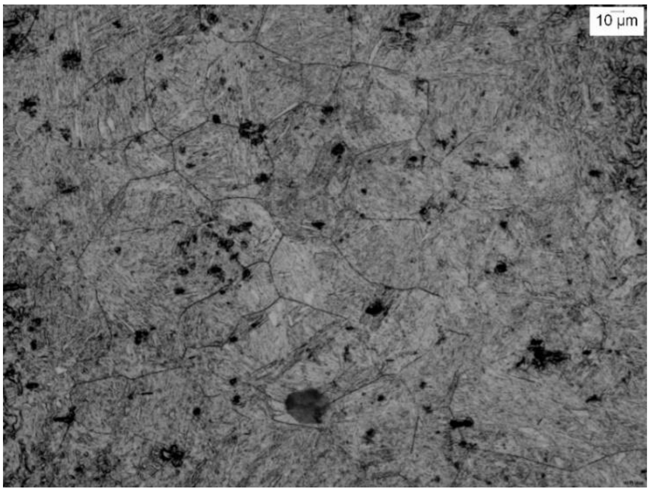

1050°C, 10 mins, 200X

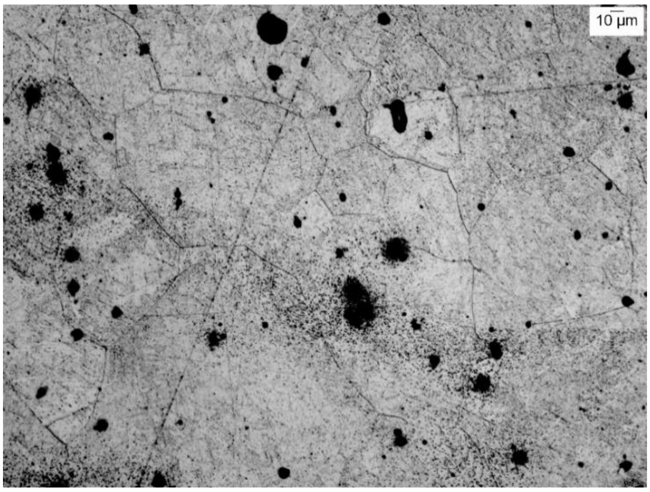

1050°C, 100 mins, 200X

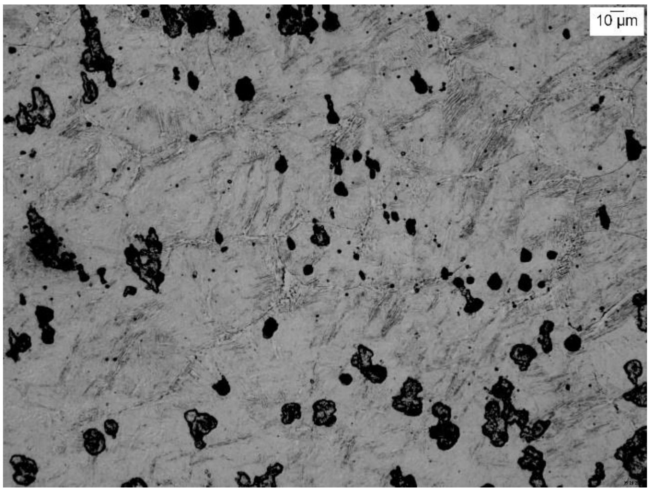

1050°C, 1000 mins, 200X

Fig 3.5: Micrograph of prior austenite grains of sample 2 after austenitizing at 1050°C and water quenching

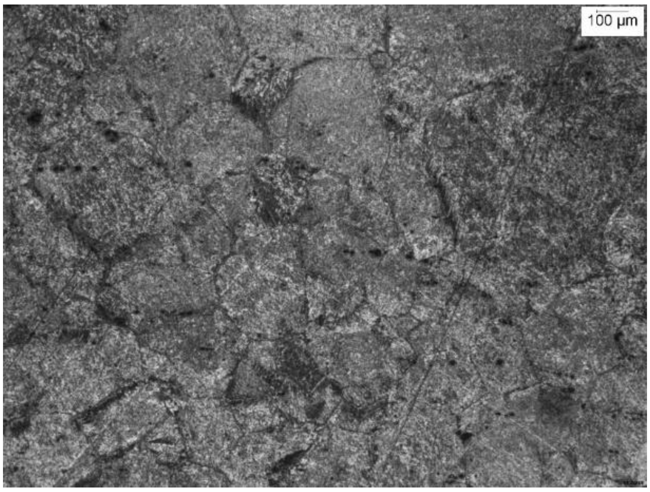

1200°C, 10 mins, 50X

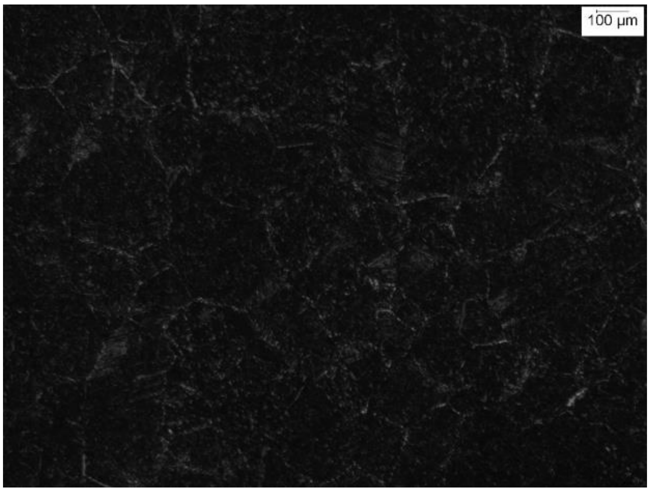

1200°C, 100 mins, 50X

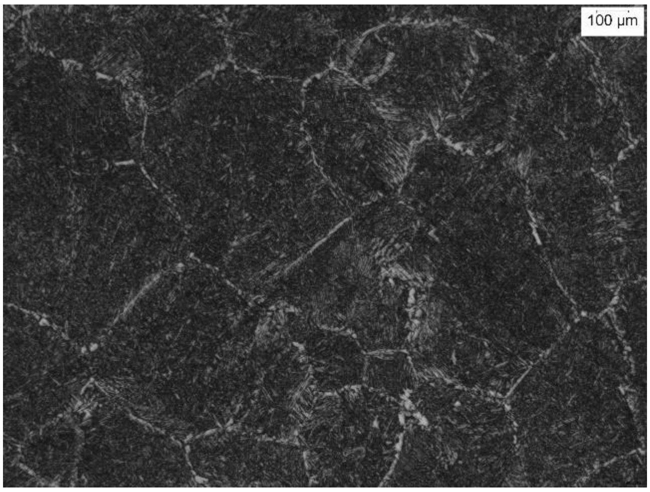

1200°C, 1000 mins, 50X

Fig 3.6: Micrograph of prior austenite grains of sample 2 after austenitizing at 1200°C and water quenching

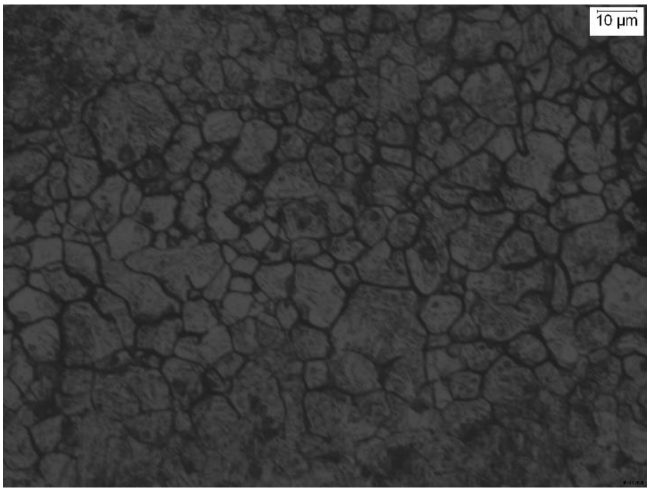

900°C, 10 mins, 500X

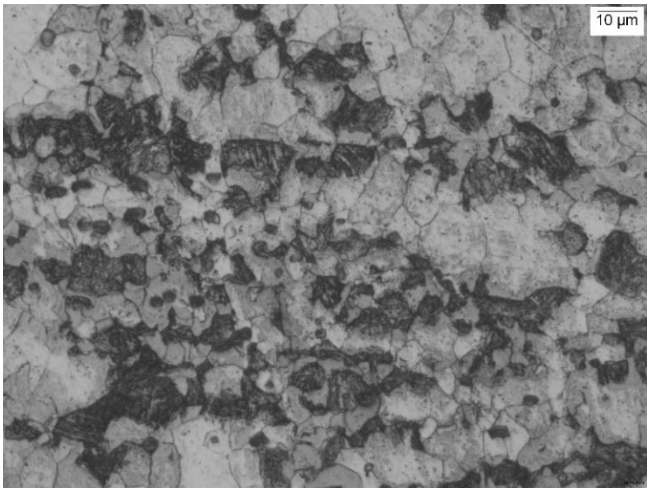

900°C, 100 mins, 500X

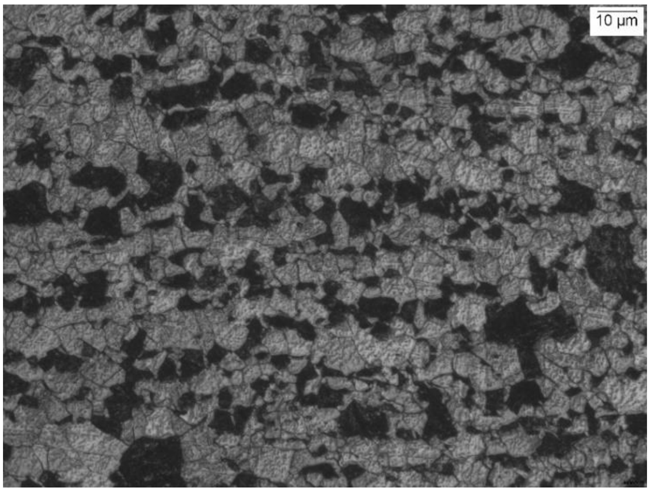

900°C, 1000 mins, 500X

Fig 3.7: Micrograph of prior austenite grains of sample 3 after austenitizing at 900°C and water quenching

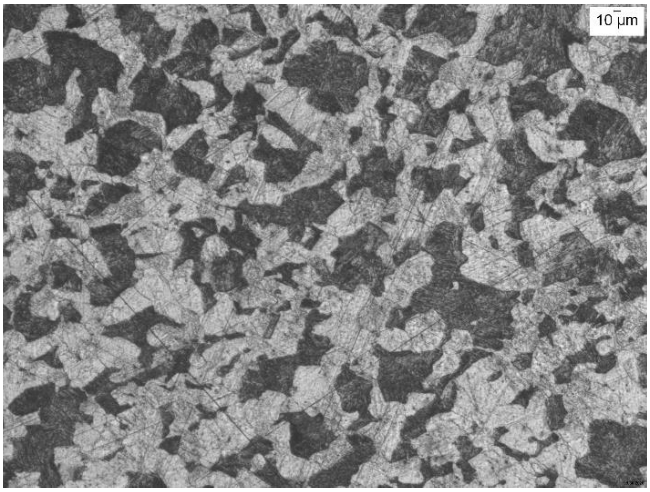

1050°C, 10 mins, 100X

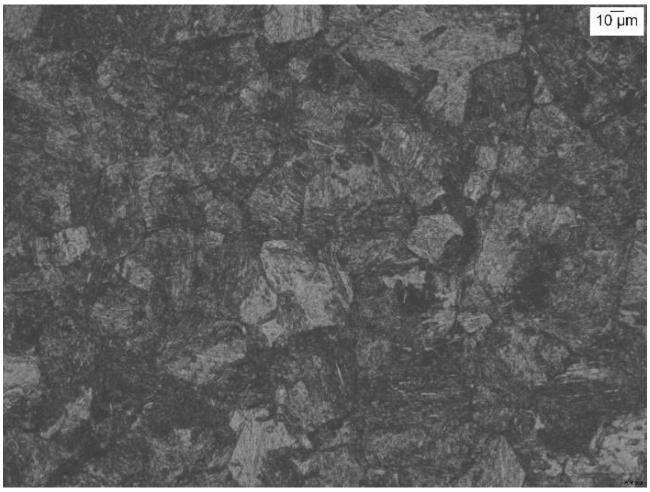

1050°C, 100 mins, 100X

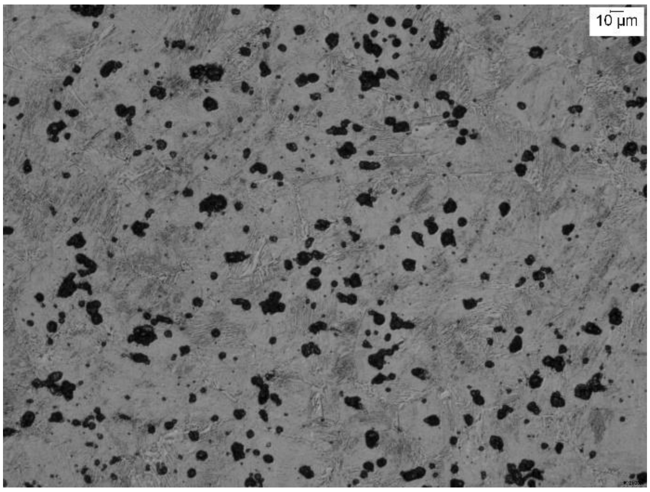

1050°C, 1000 mins, 200X

Fig 3.8: Micrograph of prior austenite grains of sample 3 after austenitizing at 1050°C and water quenching

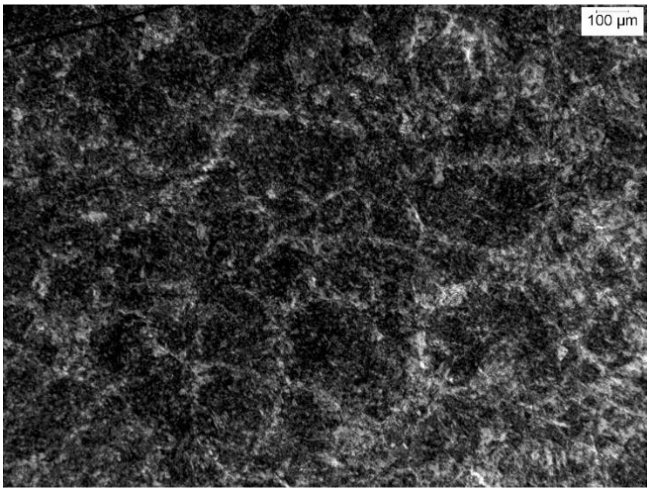

1200°C, 10 mins, 50X

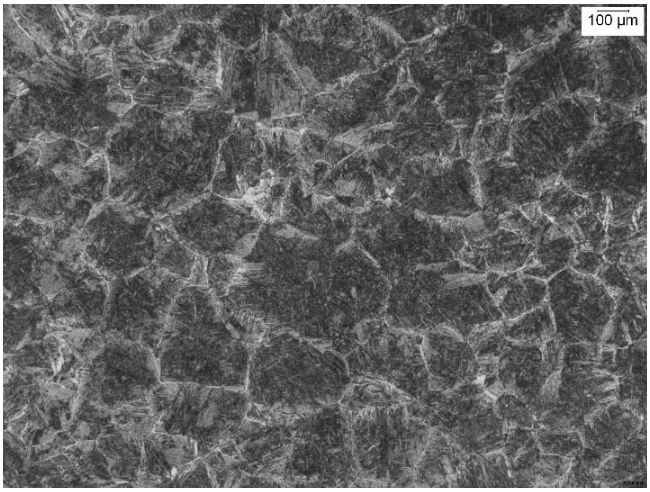

1200°C, 100 mins, 50X

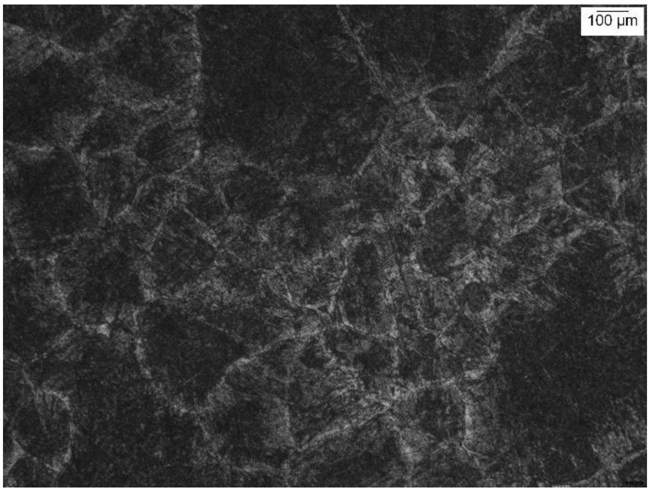

1200°C, 1000 mins, 50X

Fig 3.9: Micrograph of prior austenite grains of sample 3 after austenitizing at 1200°C and water quenching

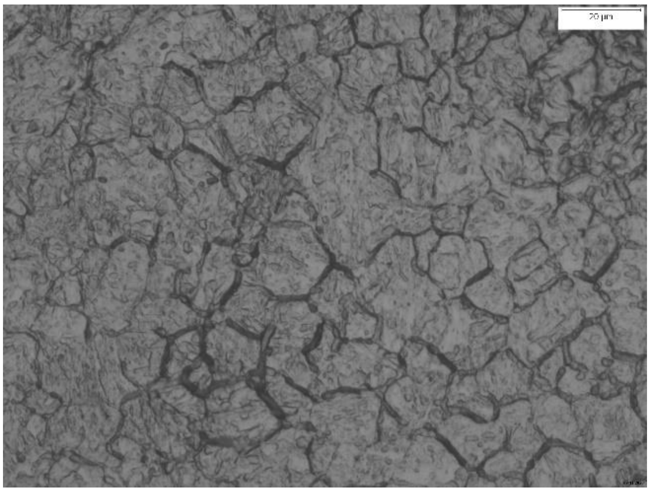

900°C, 10 mins, 500X

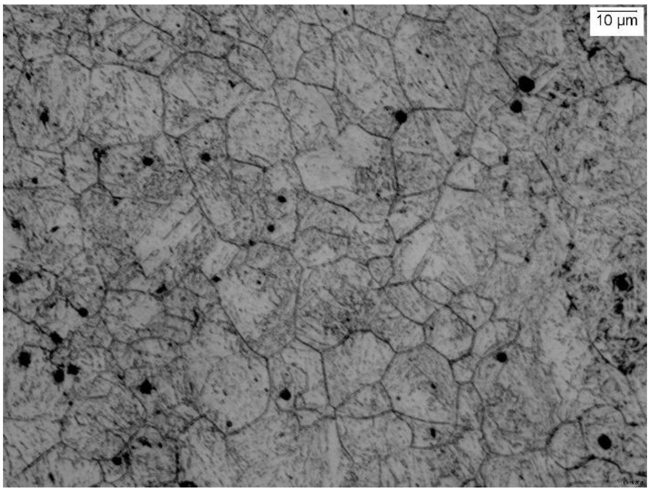

900°C, 100 mins, 500X

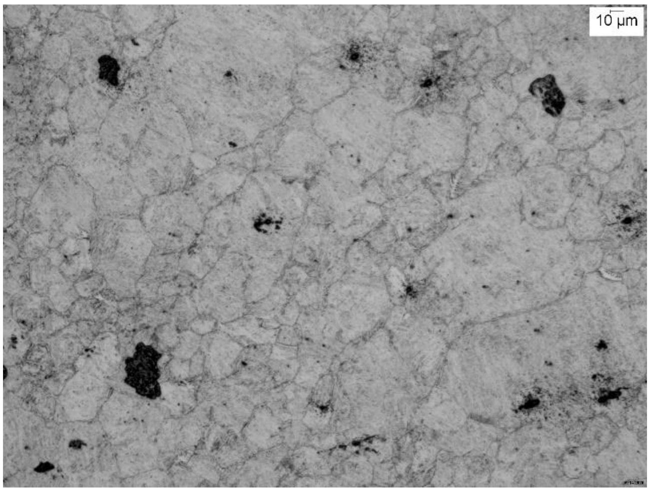

900°C, 1000 mins, 200X

Fig 3.10: Micrograph of prior austenite grains of sample 4 after austenitizing at 900°C and water quenching

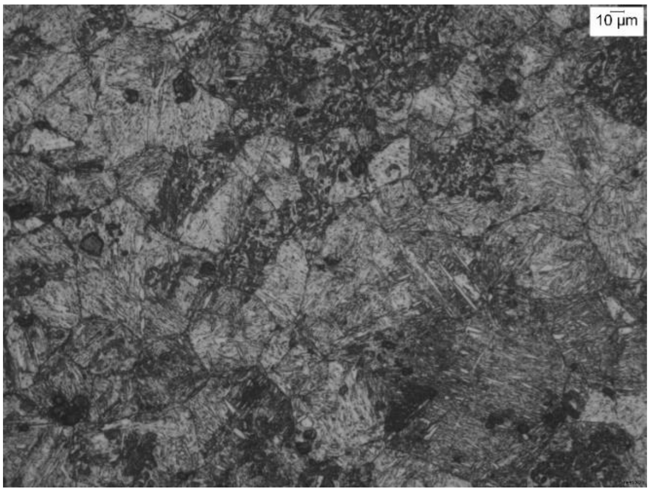

1050°C, 10 mins, 200X

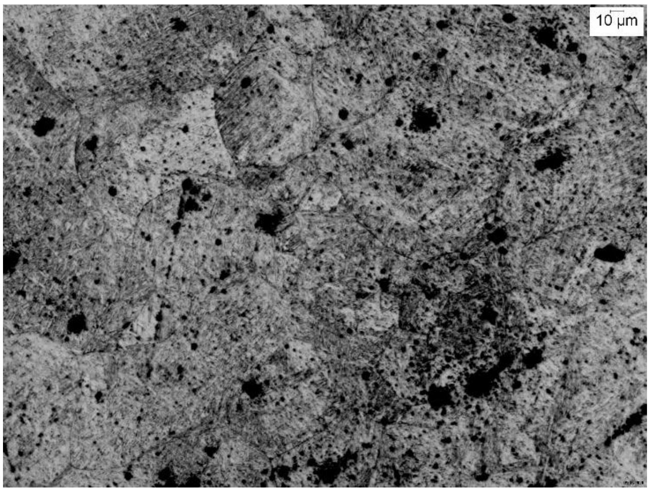

1050°C, 100 mins, 200X

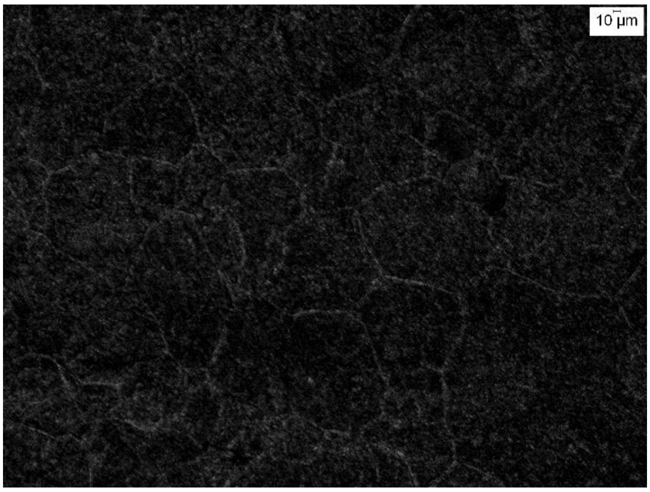

1050°C, 1000 mins, 100X

Fig 3.11: Micrograph of prior austenite grains of sample 4 after austenitizing at 1050°C and water quenching

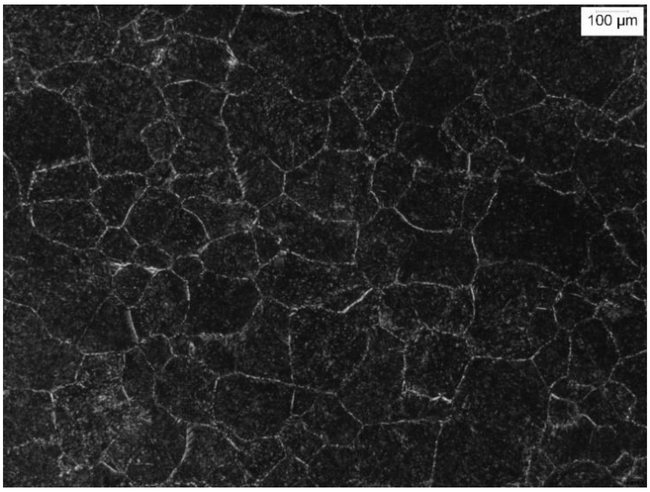

1200°C, 10 mins, 50X

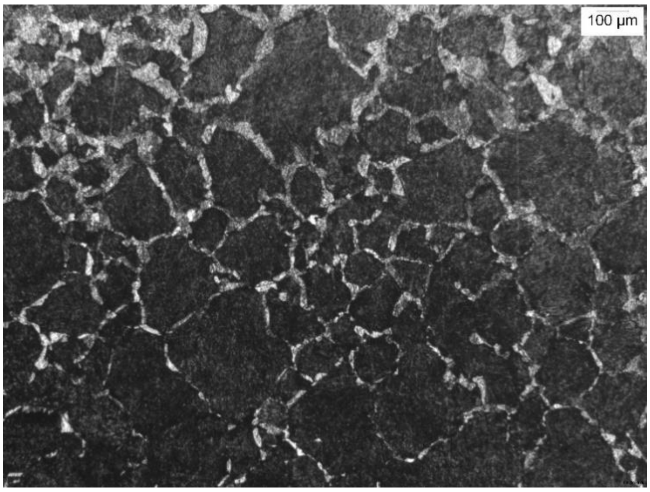

1200°C, 100 mins, 50X

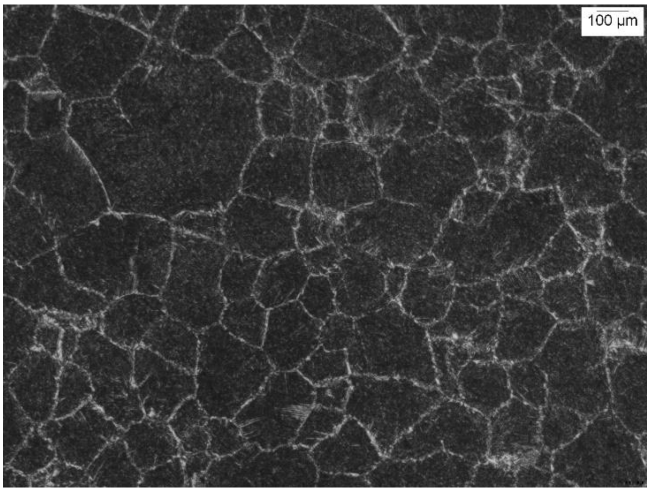

1200°C, 1000 mins, 50X

Fig 3.12: Micrograph of prior austenite grains of sample 4 after austenitizing at 1200°C and water quenching

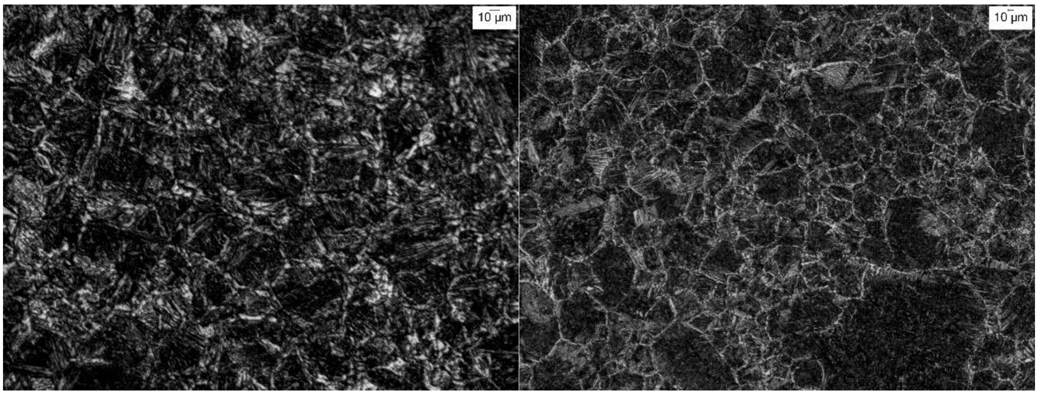

Sample 3, 975°C, 200X Sample 4, 975°C, 100X

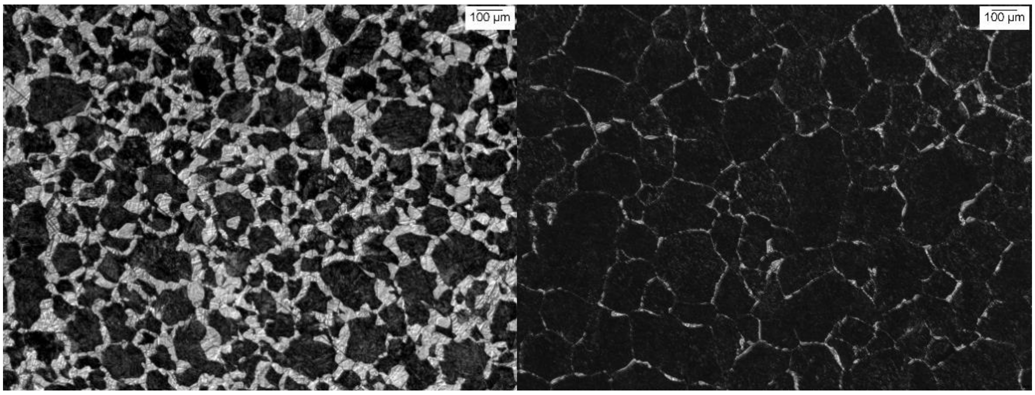

Sample 3, 1125°C, 50X Sample 4, 1125°C, 50X

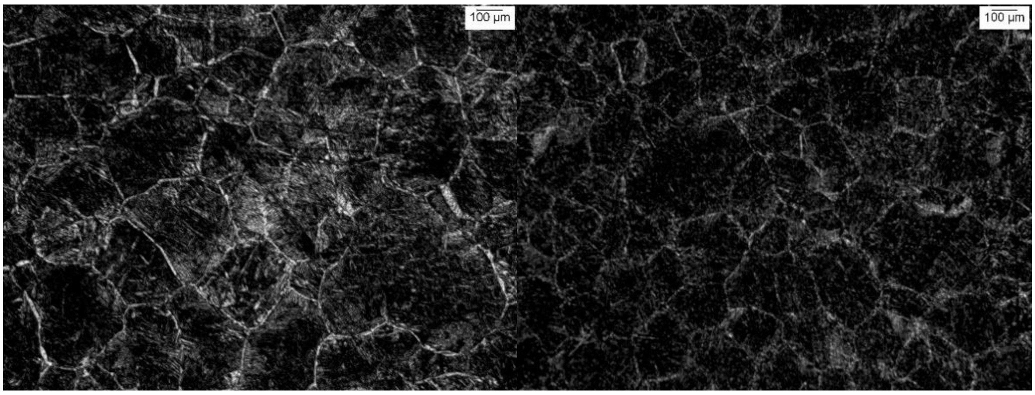

Sample 3, 1275°C, 50X Sample 4, 1275°C, 50X

Fig 3.13: Nucleation of ferrite grains on the prior austenite grain boundaries as a function of time. Samples were subjected to different austenitizing temperatures and cooled to 800°C at 15°C/min and then at 0.08°C/sec then water quenched at different temperatures

Table 3.2: Austenite grain sizes of sample 2

Austenitizing temperature	Grain size (um) 10 mins	100 mins	1000 mins
900°C	12.07	12.2	15.13
1050°C	62.69	85.69	78.64
1200°C	176.48	170.69	210.08

Table 3.3: Austenite grain sizes of sample 3

Austenitizing temperature	Grain size (um) 10 mins	100 mins	1000 mins
900°C	6.799	14.62	17.42
975°C		32	
1050°C	46.36	39.94	52
1125°C		95.37	
1200°C	176.92	162.56	175.89
1275°C		222.03	

Table 3.4: Austenite grain sizes of sample 4

Austenitizing temperature	Grain size (um) 10 mins	100 mins	1000 mins
900°C	14.52	11.03	22.06
975°C		46.62	
1050°C	49.95	83.94	88.22
1125°C		135.43	
1200°C	149.93	154.21	129.99
1275°C		182.19	

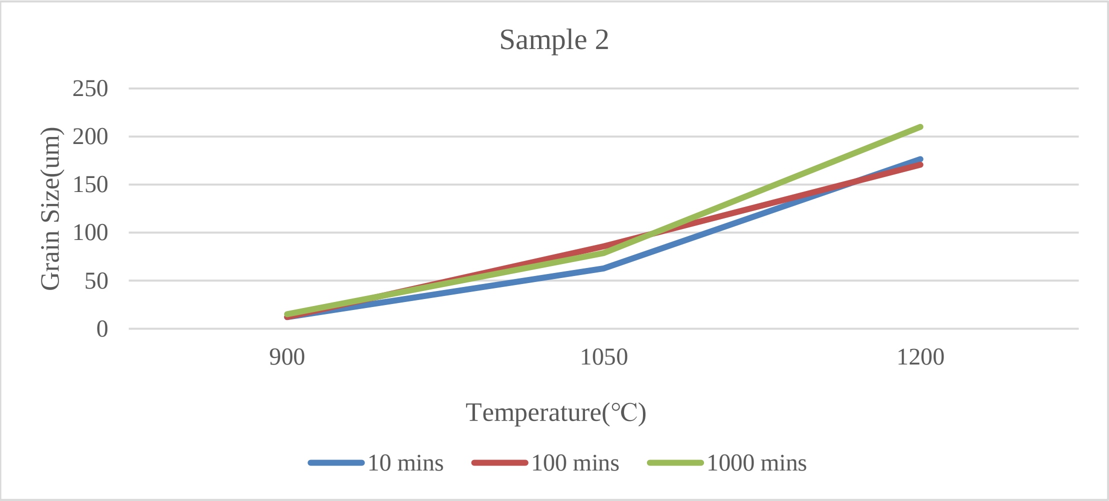

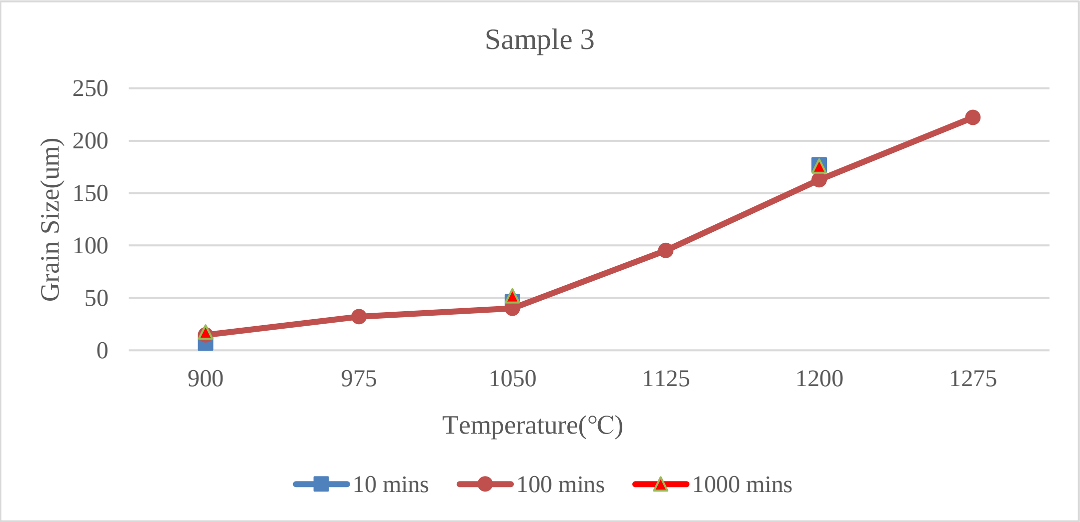

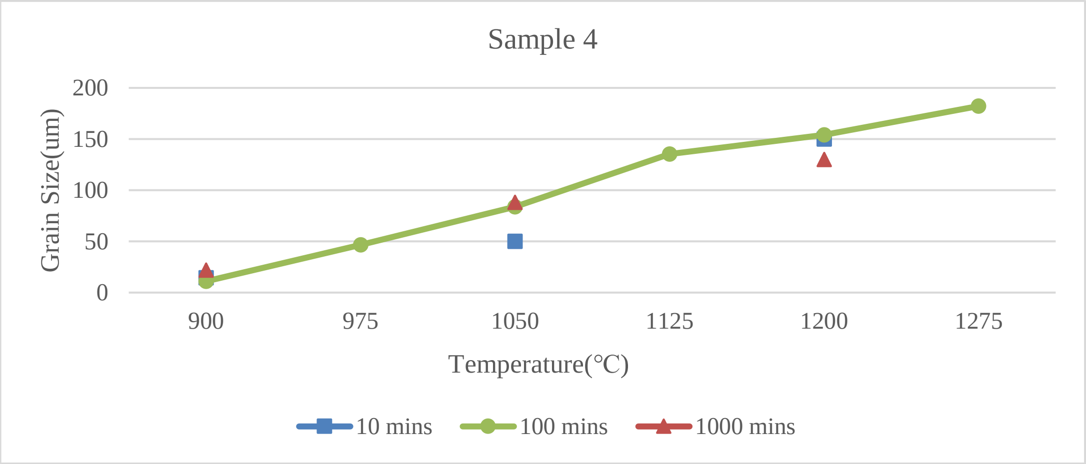

Fig 3.14: The effect of temperature on austenite grain sizes with various holding time

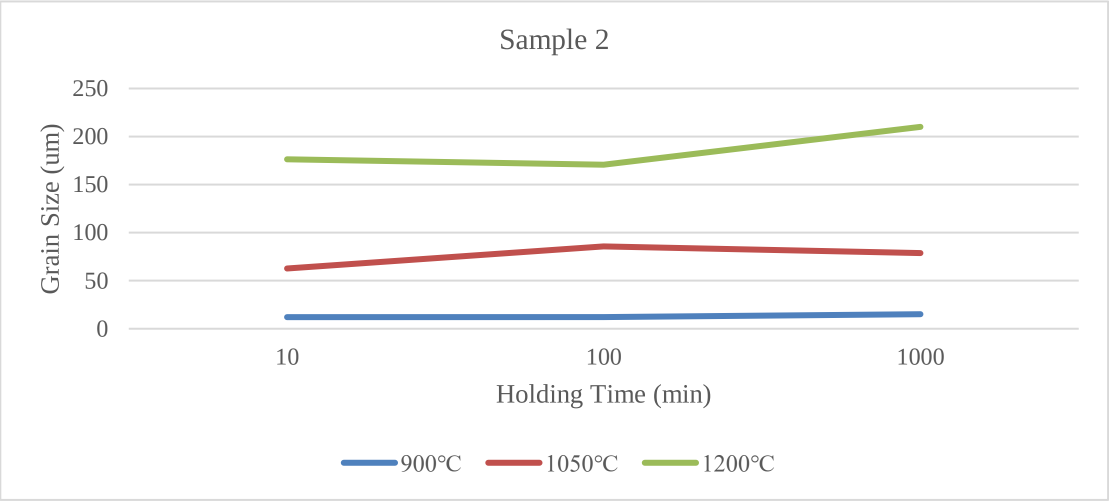

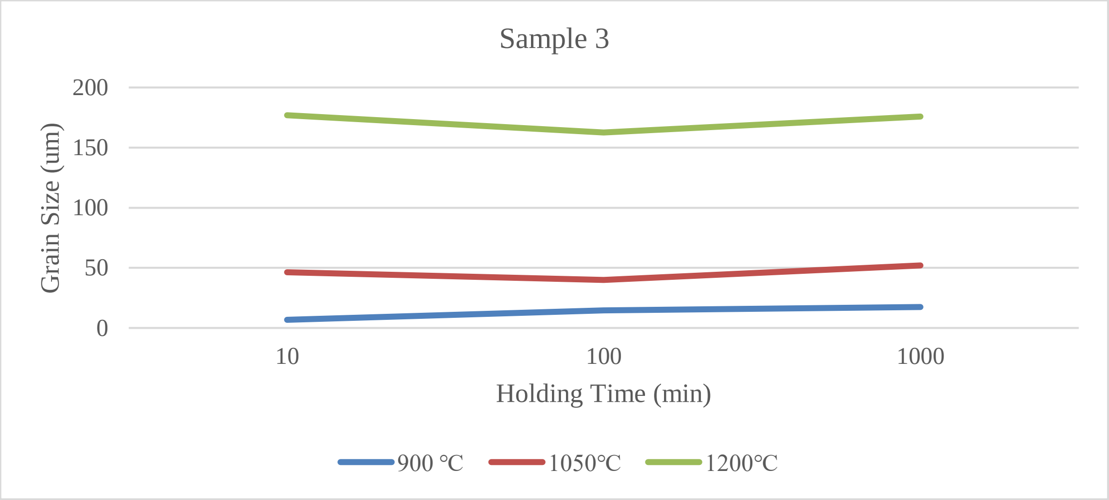

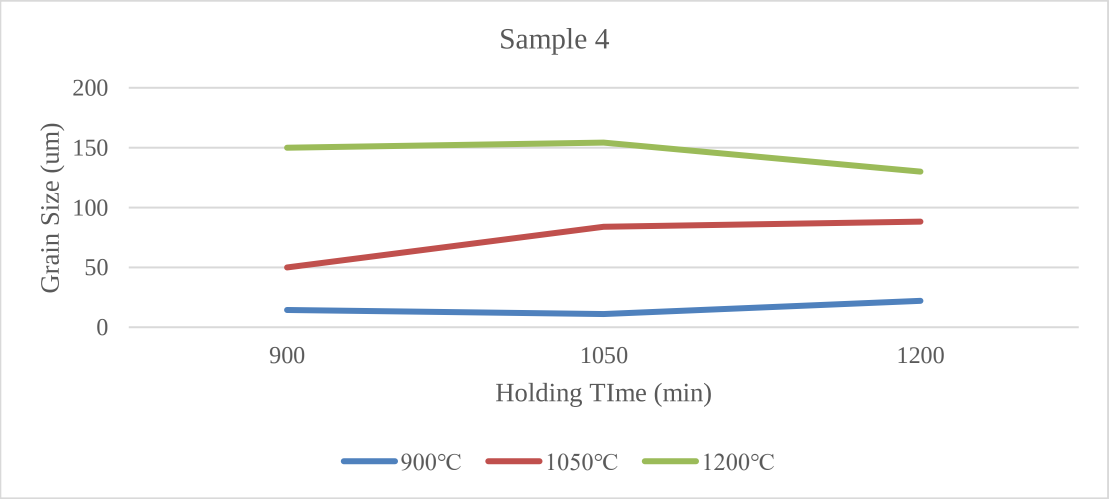

Fig 3.15: The effect of holding time on austenite grain sizes with various austenitizing temperatures

3.3 Ferrite grain growth and grain size distribution

Fig 3.17 to Fig 3.19 shows the optical micrographs of sample 2, 3 and 4 formed at various temperatures and cooling rates. The microstructure is composed of ferrite and pearlite. The ferrite grain sizes and pearlite volume fractions are shown from Table 3.5 to Table 3.10. According to the micrographs and the data, the ferrite grain size was found to increase with an increase in austenite grain size, while ferrite grain refinement was achieved with an increase in cooling rate. The temperature and cooling rate doesn't have a significant effect on pearlite volume fraction of all three samples. The ferrite grain refinement by accelerated cooling can be explained by the effect of transformation temperature on the grain size of a new phase. Ferrite formation proceeds by nucleation and growth. With an increase in cooling rate, the temperature range where austenite to ferrite transformation occurs decreases. As a result, the ferrite nucleation rate increases while the growth rate decreases, so a larger number of small-sized ferrite grains form. The ferrite grain size dependence on temperature can be explained by the number of nucleation sites. Ferrite grains mainly nucleate and grow on austenite grain boundaries as they are more energetically favorable than other areas such as inside the grain.. As temperature increases, austenite grains grow larger. As a result, the density of nucleation sites decreases, thus ferrite grain size becomes larger.

A mathematical model was proposed to predict ferrite grain size as a function of prior austenite grain size and cooling rate. To fit the experimental data, modification is made to the Saito's equation[20]. The calibrated equation is given as:

$$\ln D_{\alpha} = 0.92 + 0.44\ln D_{\gamma} - 0.1\ln CR \tag{3.4}$$

where D_{α} = ferrite grain size (um); D_{γ} = austenite grain size (um); and CR = cooling rate (°C/s).

The correlation of the predicted ferrite grain size with the measured values from optical microscopy are shown in Fig 3.16. Most predicted ferrite grain size values are within 25% error range compared to measured ferrite grain size. The prediction correlates well with the experimental values.

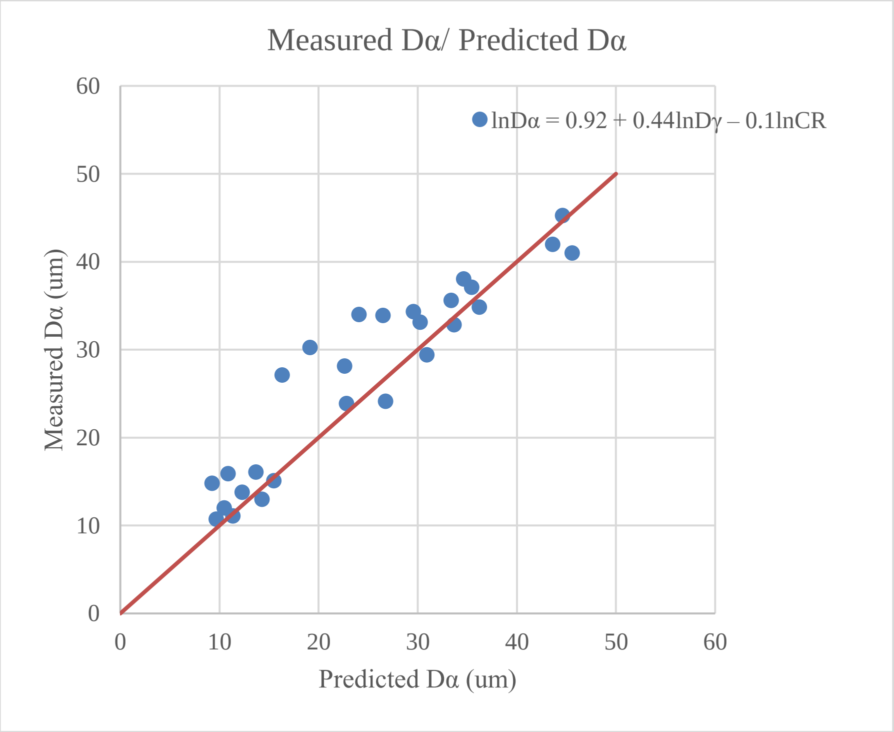

Fig 3.16: Predicted Dα vs. measured Dα

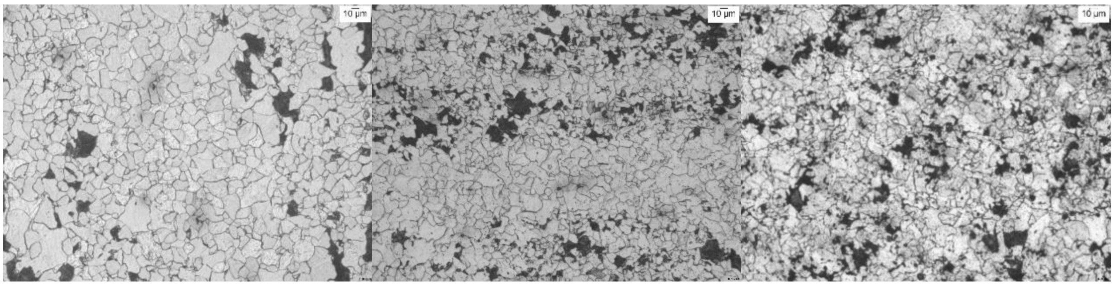

900°C, 0.1°C/min 900°C, 1°C/min 900°C, 5°C/min

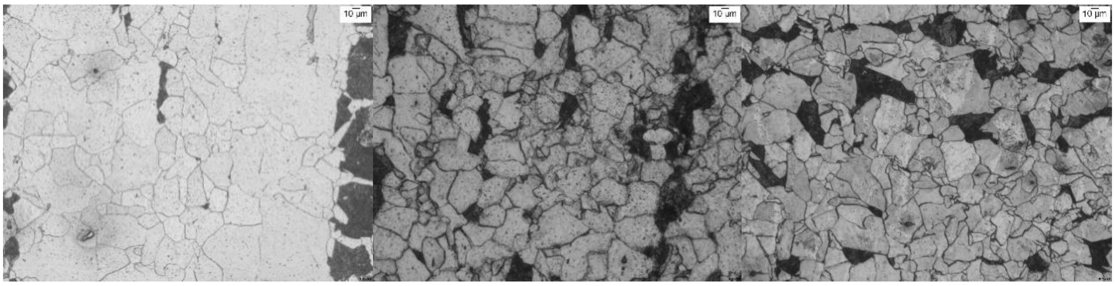

1050°C, 0.1°C/min 1050°C, 1°C/min 1050°C, 5°C/min

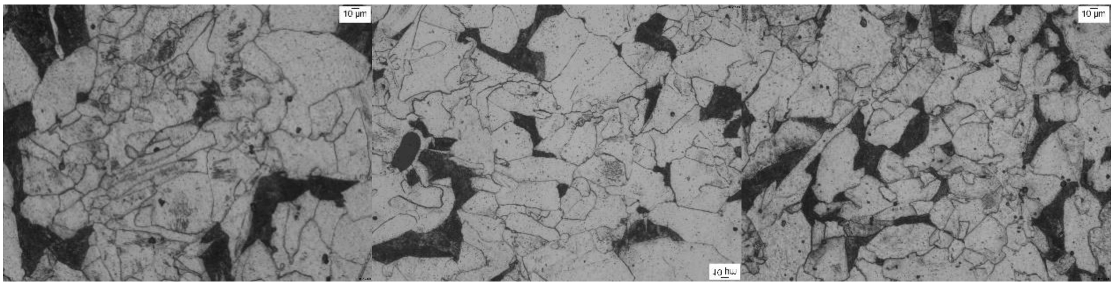

1200°C, 0.1°C/min 1200°C, 1°C/min 1200°C, 5°C/min

Fig 3.17: Microstructures of sample 2 after different heat treatments

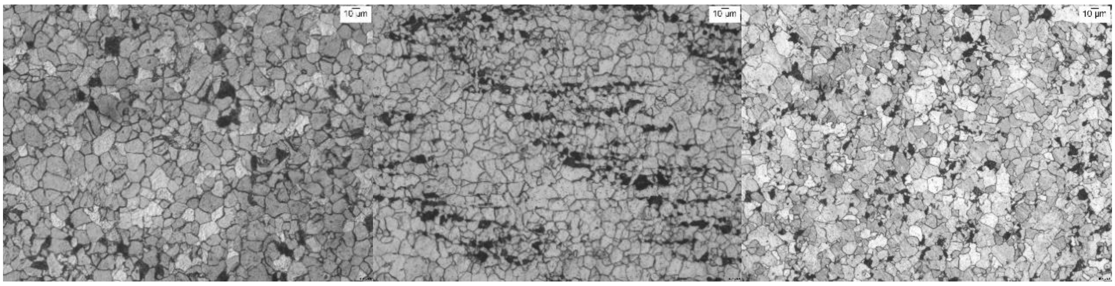

900°C, 0.1°C/min 900°C, 1°C/min 900°C, 5°C/min

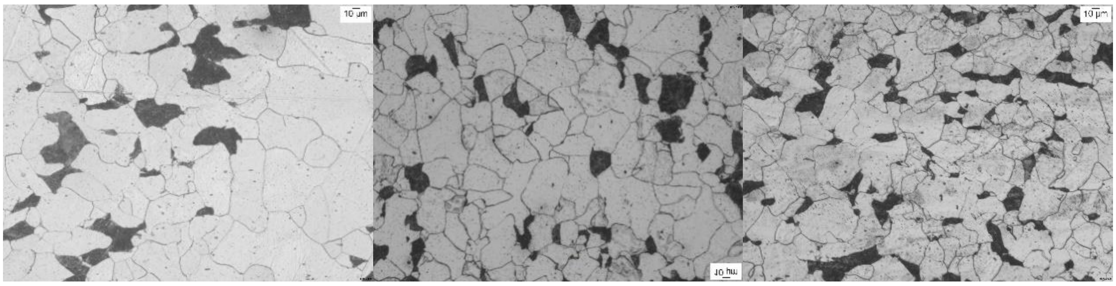

1050°C, 0.1°C/min 1050°C, 1°C/min 1050°C, 5°C/min

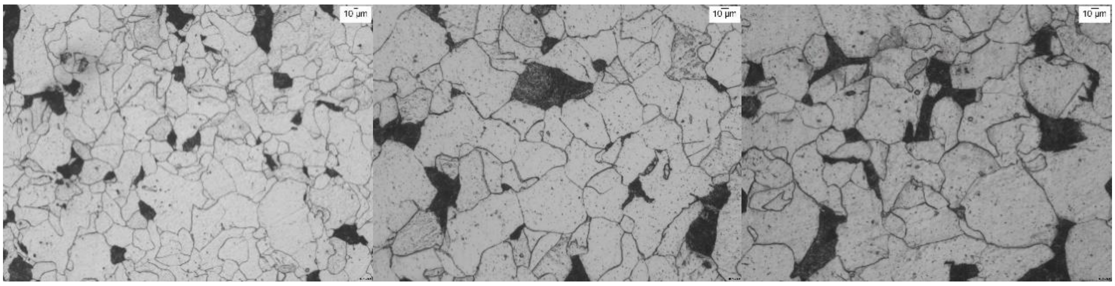

1200°C, 0.1°C/min 1200°C, 1°C/min 1200°C, 5°C/min

Fig 3.18: Microstructures of sample 3 after different heat treatments

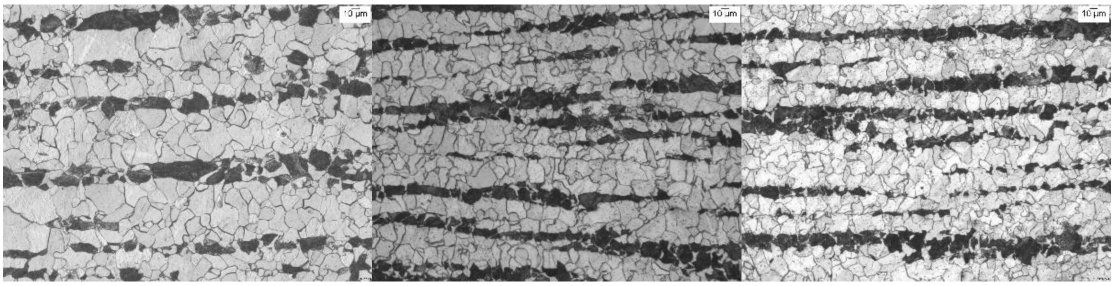

900°C, 0.1°C/min 900°C, 1°C/min 900°C, 5°C/min

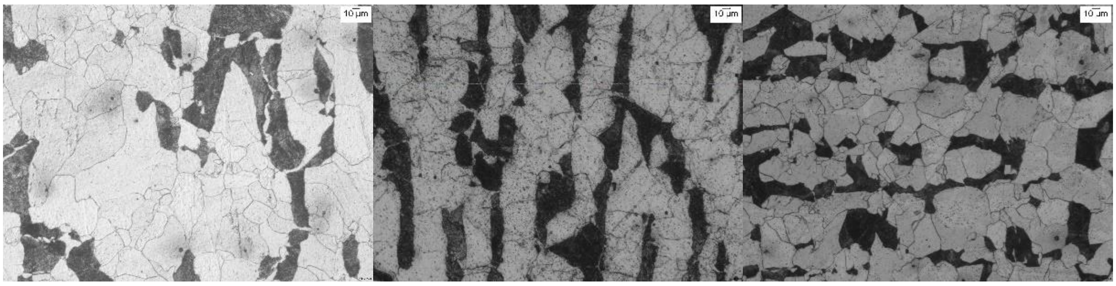

1050°C, 0.1°C/min 1050°C, 1°C/min 1050°C, 5°C/min

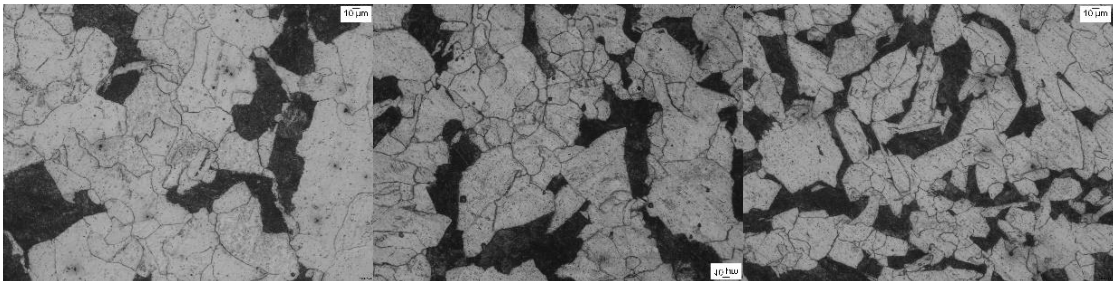

1200°C, 0.1°C/min 1200°C, 1°C/min 1200°C, 5°C/min

Fig 3.19: Microstructures of sample 4 after different heat treatments

Table 3.5: Ferrite grain sizes of sample 2

Austenitizing temperature	PAGS (um)	Ferrite grain size (um)		
		0.1°C/min	1°C/min	5°C/min
900°C	12.2	12.98	11.09	10.74
1050°C	85.69	32.84	24.14	23.9
1200°C	170.69	41	34.85	29.41

Table 3.6: Ferrite grain sizes of sample 3

Austenitizing temperature	PAGS (um)	Ferrite grain size (um)		
		0.1°C/min	1°C/min	5°C/min
900°C	14.62	15.09	13.79	12.03
1050°C	39.94	34.01	30.25	27.12
1200°C	162.56	45.28	37.09	33.13

Table 3.7: Ferrite grain sizes of sample 4

Austenitizing temperature	PAGS (um)	Ferrite grain size (um)		
		0.1°C/min	1°C/min	5°C/min
900°C	11.03	16.09	15.91	14.81
1050°C	83.94	35.62	33.89	28.13
1200°C	154.21	41.99	38.04	34.34

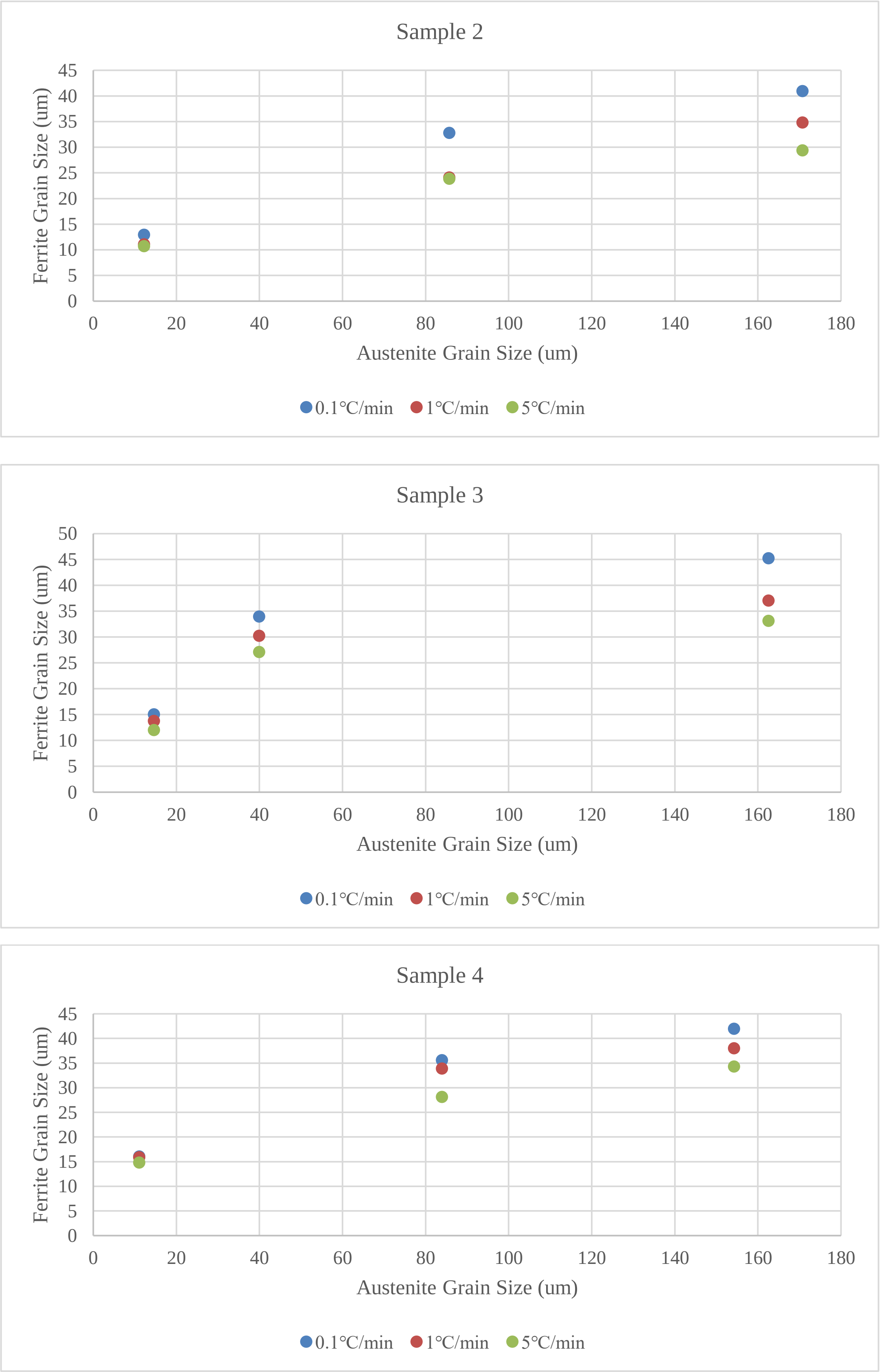

Fig 3.20: Effect of prior austenite grain sizes and cooling rate on ferrite grain sizes

Table 3.8: Pearlite volume fraction of sample 2

Austenitizing	Pearlite Volume Fraction(%)		
temperature	0.1°C/min	1°C/min	5°C/min
900°C	9.8	10.12	15.46
1050°C	14.95	18.69	16.3
1200°C	17.68	13.86	18.8

Table 3.9: Pearlite volume fraction of sample 3

Austenitizing	Pearlite Volume Fraction(%)		
temperature	0.1°C/min	1°C/min	5°C/min
900°C	7.03	7.99	5.96
1050°C	10.13	9.79	9.2
1200°C	9.03	10.79	9.12

Table 3.10: Pearlite volume fraction of sample 4

Austenitizing	Pearlite Volume Fraction(%)		
temperature	0.1°C/min	1°C/min	5°C/min
900°C	23	24.86	26.91
1050°C	25.85	30.31	27.7
1200°C	27.4	23.1	30.64

From optical micrographs, it is noticeable that for samples which are heat treated at different temperatures, the grain size distributions are not the same. At 900°C, all three steels show low variation in grain sizes, while at 1050°C and 1200°C, mixed coarse and fine-grain structure is observed. Hence special attention is paid to the samples heat treated at higher temperatures using EBSD analysis. Non-heat-treated sample 3 and sample 3 heat treated at 900°C and 0.1°C/min are studied for sake of comparison. Fig 3.21 to Fig 3.23 shows the band contrast maps and Fig 3.24 to Fig 3.26 shows the Euler color maps.

The grain size distribution measured by EBSD analysis is plotted in terms of number frequency and area frequency, and the results are shown in Fig 3.27 to Fig 3.30.

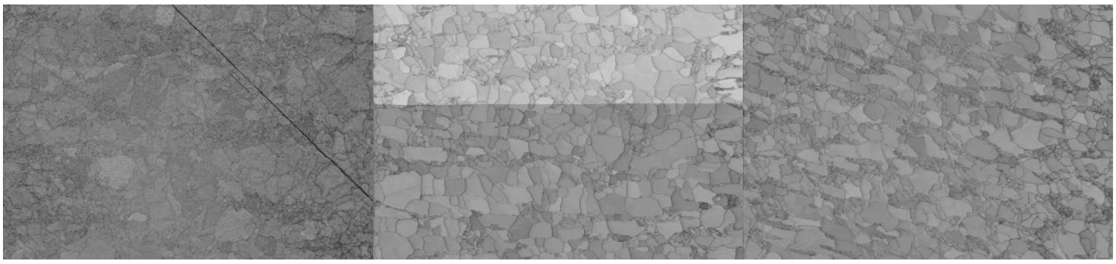

2, 1050°C, 0.1°C/min 3, 1050°C, 0.1°C/min 4, 1050°C, 0.1°C/min

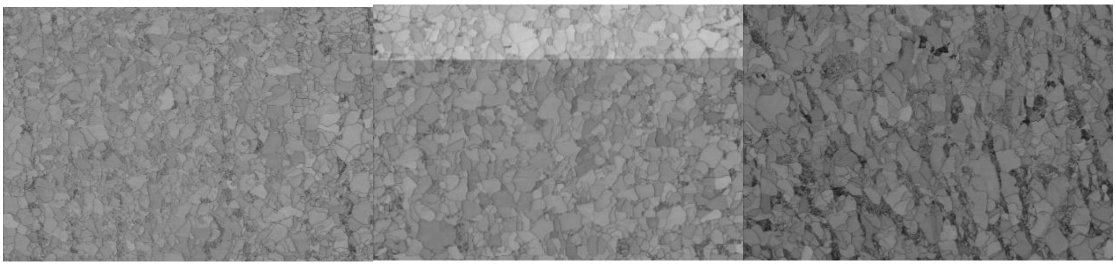

2, 1050°C, 1°C/min 3, 1050°C, 1°C/min 4, 1050°C, 1°C/min

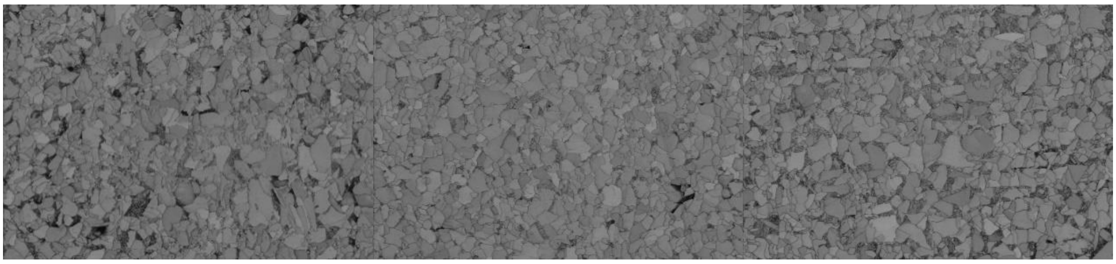

2, 1050°C, 5°C/min 3, 1050°C, 5°C/min 4, 1050°C, 5°C/min

Fig 3.21: Band contrast maps of steels heat treated at 1050°C

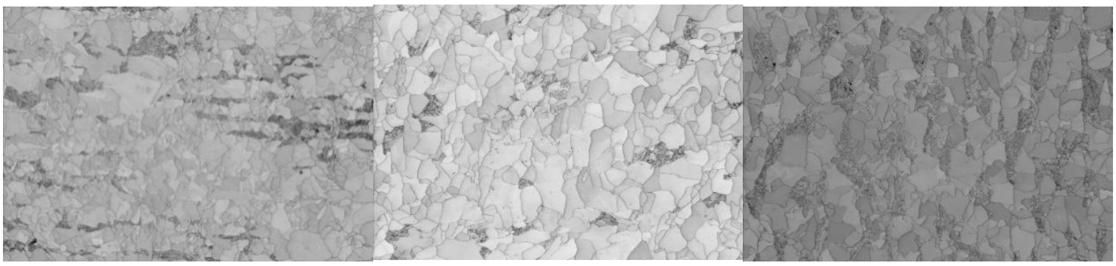

2, 1200°C, 0.1°C/min 3, 1200°C, 0.1°C/min 4, 1200°C, 0.1°C/min

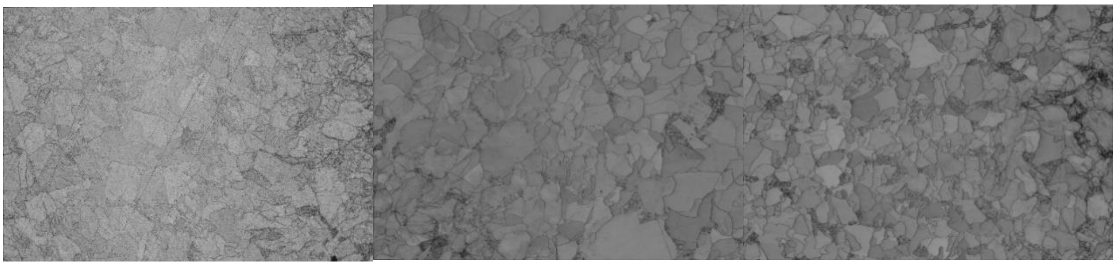

2, 1200°C, 1°C/min 3, 1200°C, 1°C/min 4, 1200°C, 1°C/min

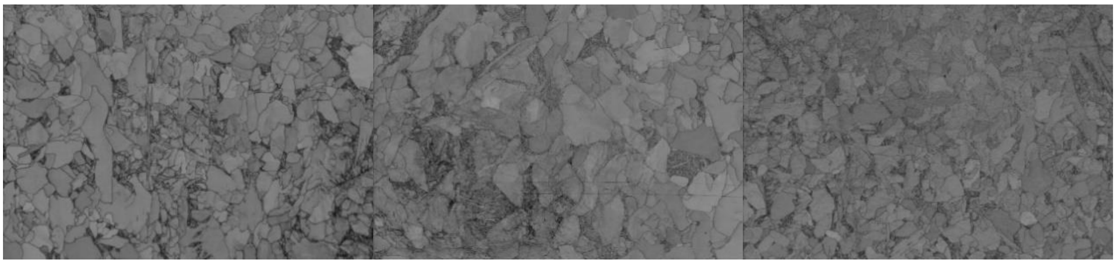

2, 1200°C, 5°C/min 3, 1200°C, 5°C/min 4, 1200°C, 5°C/min

Fig 3.22: Band contrast maps of steels heat treated at 1200°C

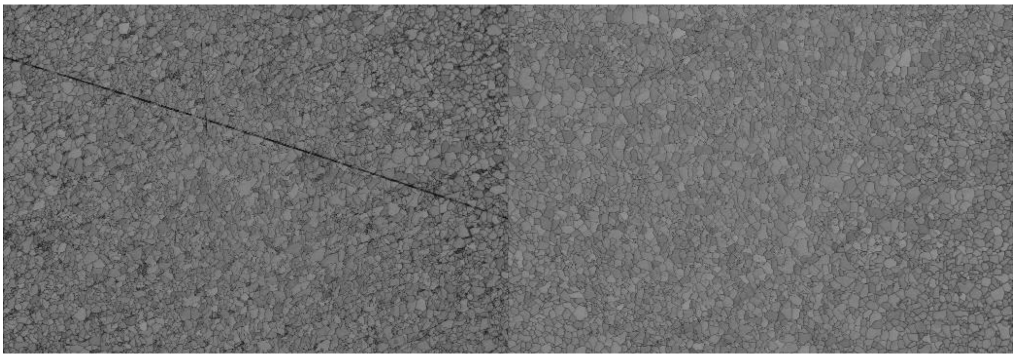

(a) (b)

Fig 3.23: Band contrast maps of (a) non-heat treated sample 3; (b) sample 3 heat treated at 900°C and 0.1°C/min, as a comparison

2, 1050°C, 0.1°C/min 3, 1050°C, 0.1°C/min 4, 1050°C, 0.1°C/min

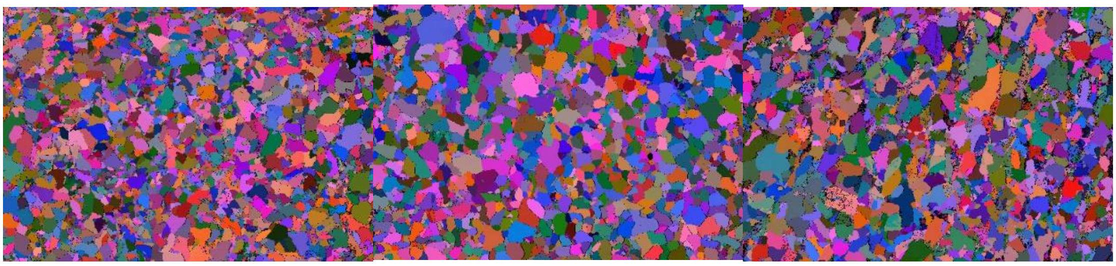

2, 1050°C, 1°C/min 3, 1050°C, 1°C/min 4, 1050°C, 1°C/min

2, 1050°C, 5°C/min 3, 1050°C, 5°C/min 4, 1050°C, 5°C/min

Fig 3.24: Euler color maps of steels heat treated at 1050°C

2, 1200°C, 0.1°C/min 3, 1200°C, 0.1°C/min 4, 1200°C, 0.1°C/min

2, 1200°C, 1°C/min 3, 1200°C, 1°C/min 4, 1200°C, 1°C/min

2, 1200°C, 5°C/min 3, 1200°C, 5°C/min 4, 1200°C, 5°C/min

Fig 3.25: Euler color maps of steels heat treated at 1200°C

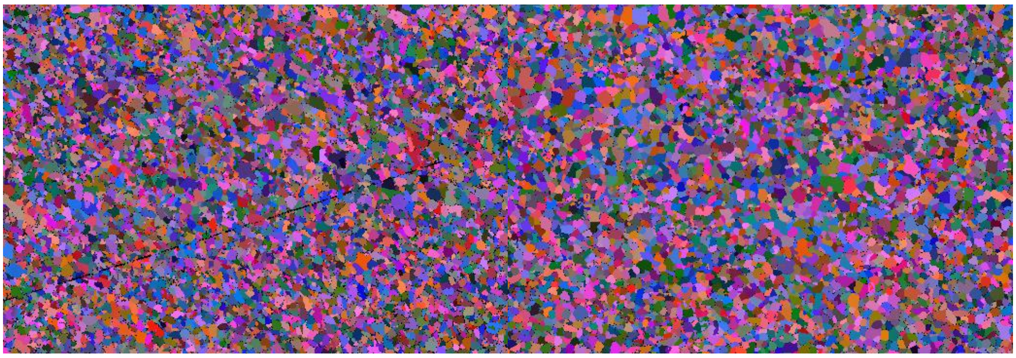

(a) (b)

Fig 3.26: Euler color maps of (a) non-heat treated sample 3; (b) sample 3 heat treated at 900°C and 0.1°C/min, as a comparison

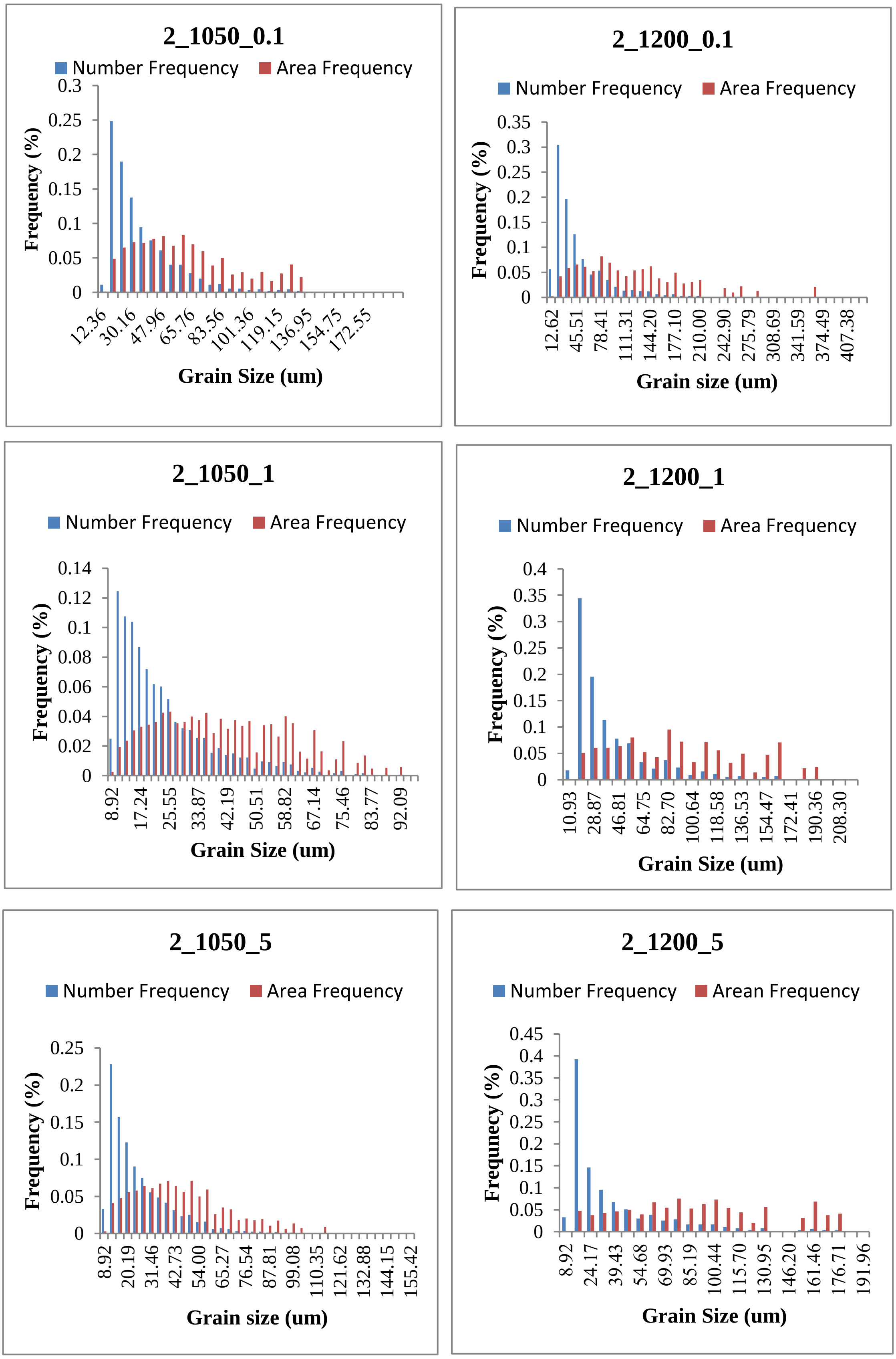

Fig 3.27: Ferrite-grain size distributions of sample 2 in terms of number-frequency and area-frequency histograms

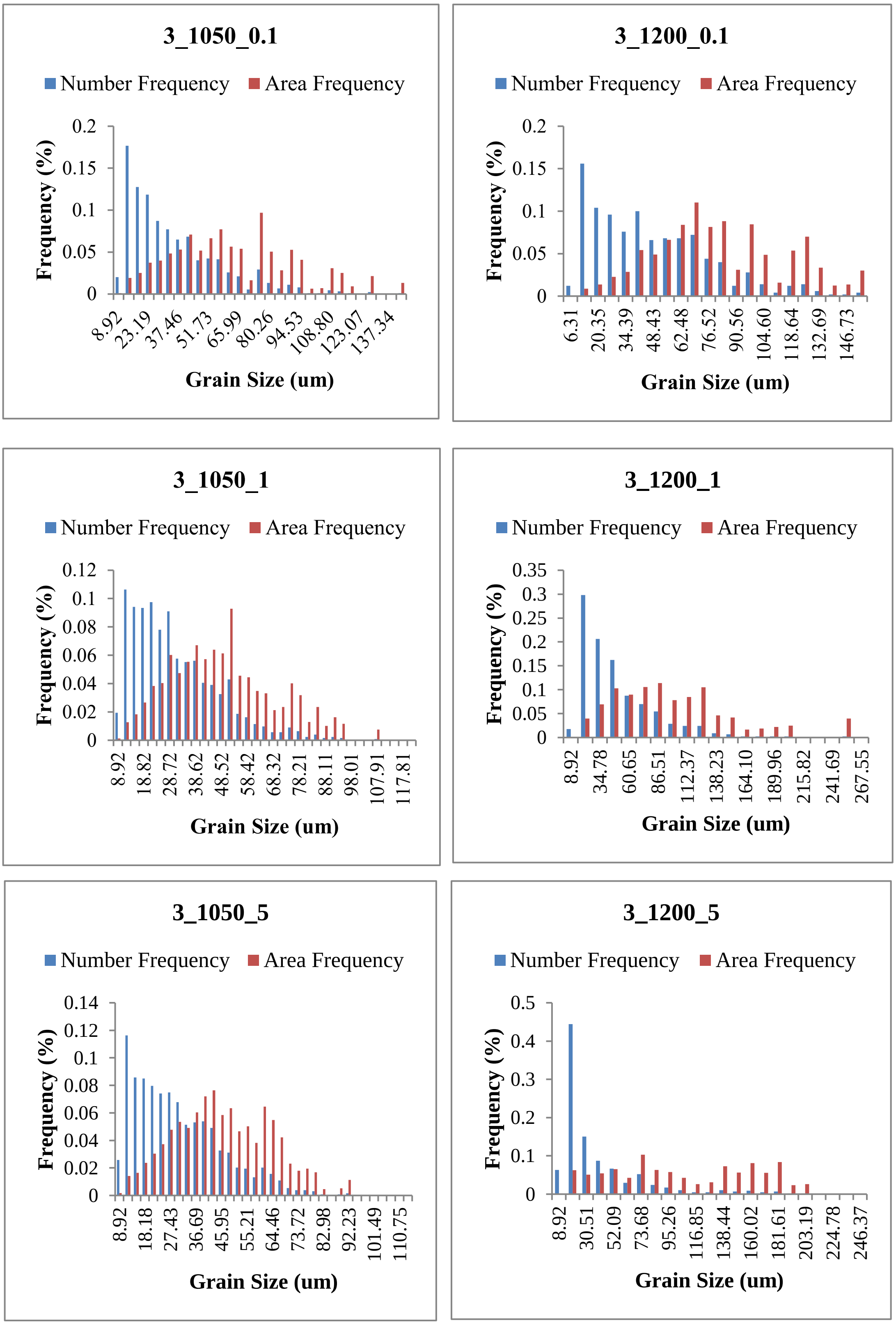

Fig 3.28: Ferrite-grain size distributions of sample 3 in terms of number-frequency and area-frequency histograms

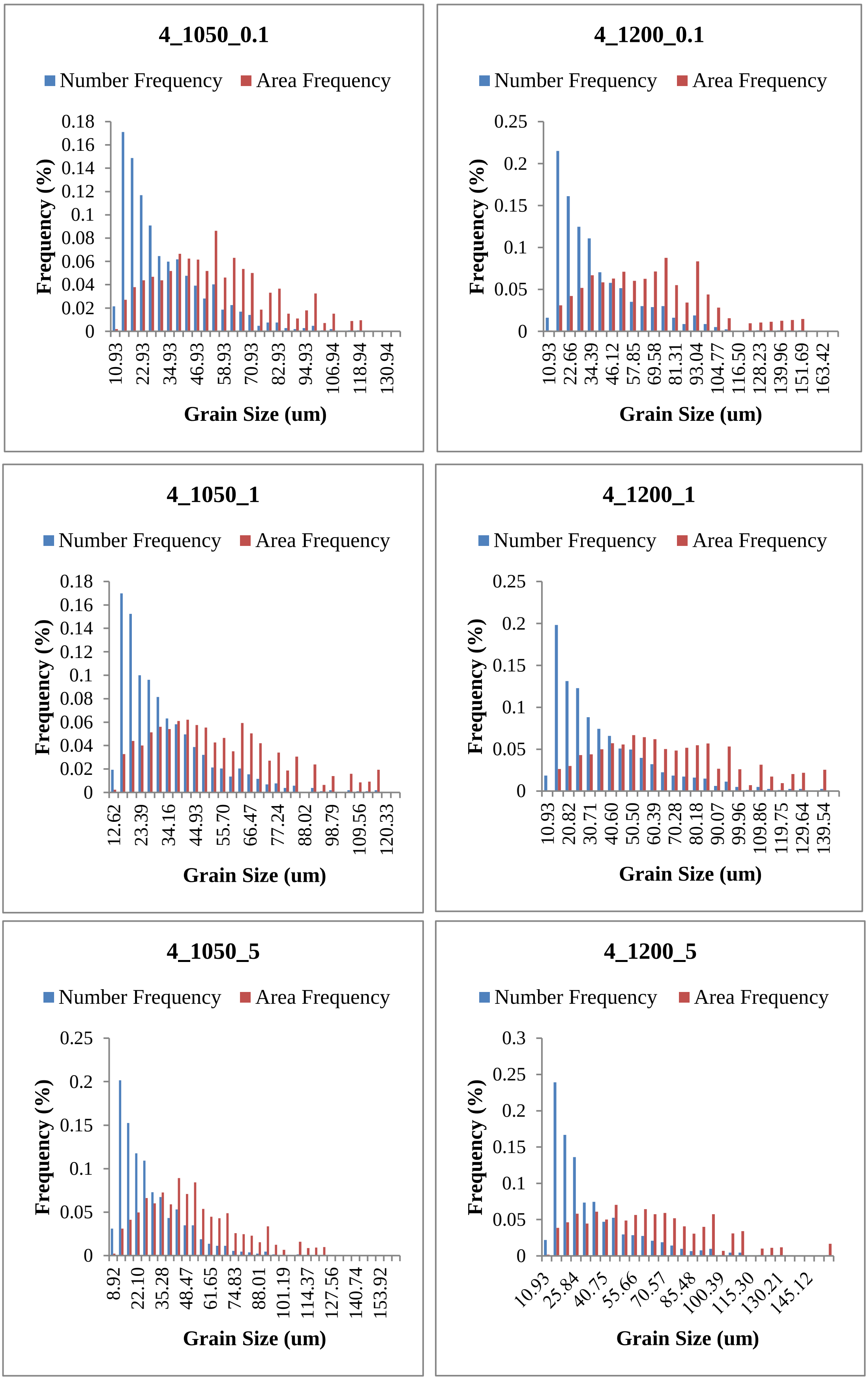

Fig 3.29: Ferrite-grain size distributions of sample 4 in terms of number-frequency and area-frequency histograms

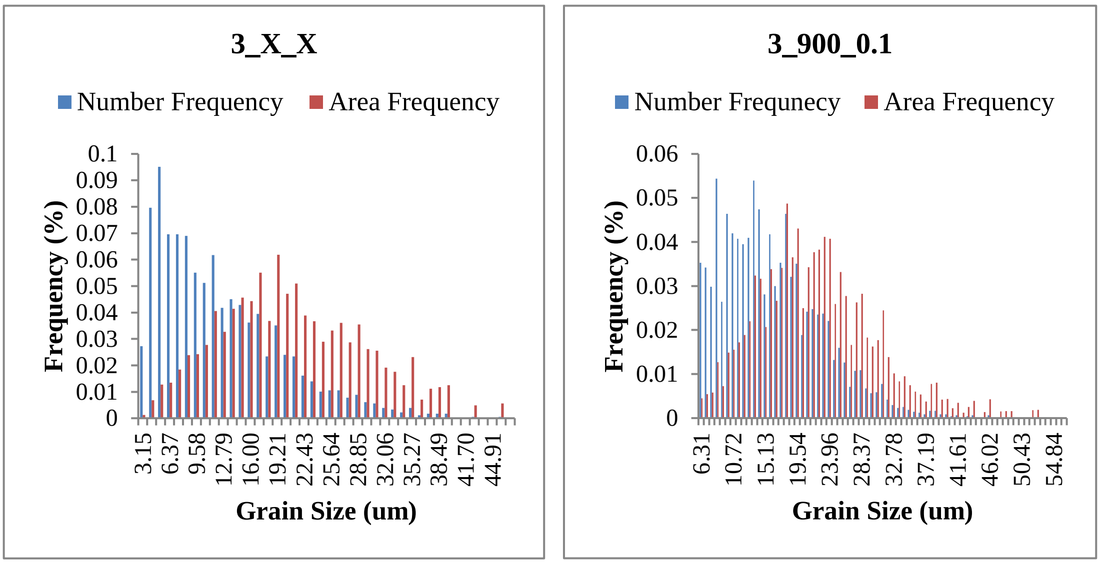

(a) (b)

Fig 3.30: Ferrite grain size distributions of (a) non-heat treated sample 3; (b) sample 3 heat treated at 900°C and 0.1°C/min in terms of number-frequency and area-frequency histograms, as a comparison

Apparently, the histogram of non-heat treated sample 3 and sample 3 heat treated at 900°C and 0.1°C/min in terms of number-frequency and area-frequency both shows a unimodal distribution of ferrite grain size (Fig 3.30). However, at 1050°C and 1200°C, as indicated by the histograms, there is an increase in spread of the grain size distribution when compared to the non-heat treated conditions and those at 900°C, which are consistent with the observations from optical microscopy.

The standard deviation of the ferrite grain sizes of non-heat treated sample 3 and sample 3 heat treated at 900°C and 0.1°C/min is 6.45 μm and 6.98 μm, respectively. In comparison, the standard deviation of the ferrite grain sizes of three steels heat treated at 1050°C and 1200°C ranges from 15 μm to 38 μm, showing a sharp increase in spread of the grain size distribution.

3.4 Vickers hardness and dislocation density

3.4.1 Measurements of Vickers hardness

The results of measured Vickers hardness values are summarized in Table 3.11 to Table 3.13 for all three samples. The HV of non-heat treated sample 2, 3, and 4 is 175.67, 173.05, 158.42, respectively. The data indicate that the Vickers hardness of all samples experience an obvious reduction after being heat treated. Among the samples which underwent the same heat treatment, the Vickers hardness of sample 2 and sample 4 are very close, while the HV of sample 3 is slightly lower. For each sample, the effect of heat treatment on HV is the same. The Vickers hardness of samples exhibits an increase with an increasing cooling rate at various temperatures. The temperature has different effects on Vickers hardness at various cooling rates. For the cooling rate at 0.1°C/min and 1°C/min, the Vickers hardness of all three steels doesn’t exhibit considerable change when temperature increases from 900°C to 1050°C and 1200°C. However, for the cooling rate of 5°C/min, the Vickers hardness increases as temperature increases from 900°C to 1050°C and 1200°C.

Table 3.11: Vickers hardness of sample 2

Austenitizing	HV		
temperature	0.1°C/min	1°C/min	5°C/min
900°C	112.31	129.12	134.14
1050°C	120.27	129.82	144.67
1200°C	117.49	132.66	168.96

Table 3.12: Vickers hardness of sample 3

Austenitizing	HV		
temperature	0.1°C/min	1°C/min	5°C/min
900°C	111.14	123.36	123.72
1050°C	107.1	120.21	126.01
1200°C	107.97	123.65	144.22

Table 3.13: Vickers hardness of sample 4

Austenitizing	HV		
temperature	0.1°C/min	1°C/min	5°C/min
900°C	114.55	128.68	135.52
1050°C	106.7	130.08	145.51
1200°C	114.84	125.68	151.44

3.4.2 Estimation of dislocation density

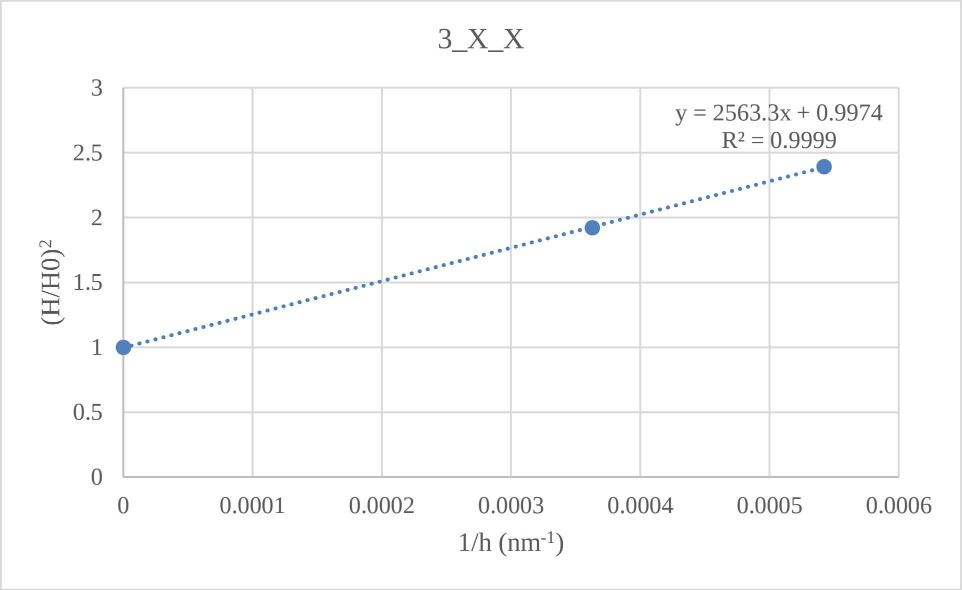

Fig 3.31: Indentation size effect and fitting of Equation 2.3 for sample 3 (non-heat treated)

Vickers hardness values, retrieved from the indentation tests, increase with decreasing indentation depth as shown in Fig 3.31, taking non-heat-treated sample 3 as an example. By fitting Equation 2.3 to the experimental Vickers hardness values (see the regression curve in Figure 3.31), a value of h* ~2563.3 nm could be obtained. By introducing all these known values into Equation, a dislocation density of 5.62 × 109cm^{-2} is obtained. The dislocation density of sample 2 and 4 was approximately estimated as 6.18 × 109cm^{-2} and 5.01 × 109cm^{-2} respectively using the same method. All the estimated dislocation density values of heat treated samples are shown in Table 3.14 to Table 3.16. Dislocation strengthening contributed by the dislocations will be calculated in the following parts using data below.

Table 3.14: Dislocation density of sample 2

Austenitizing temperature	ρ (cm^{-2}) 0.1°C/min	1°C/min	5°C/min
900°C	6.08E+09	8.00E+09	5.87E+09
1050°C	5.11E+09	4.45E+09	3.99E+09
1200°C	2.87E+09	4.90E+09	7.13E+09

Table 3.15: Dislocation density of sample 3

Austenitizing temperature	ρ (cm^{-2}) 0.1°C/min	1°C/min	5°C/min
900°C	4.08E+09	3.64E+09	5.62E+09
1050°C	3.20E+09	5.29E+09	4.67E+09
1200°C	3.57E+09	5.72E+09	6.59E+09

Table 3.16: Dislocation density of sample 4

Austenitizing temperature	ρ (cm^{-2}) 0.1°C/min	1°C/min	5°C/min
900°C	4.63E+09	8.83E+09	1.43E+10
1050°C	7.56E+09	8.76E+09	1.02E+10
1200°C	4.15E+09	4.78E+09	8.99E+09

3.5 Rockwell hardness

The average Hardness (HRB) measured by automated and manual tester for three samples are shown in Table 3.17 to Table 3.22. The results from manual tester are consistent with those from automatic measuring. The HRB from automatic tester of three non-heat treated samples is 84.33, 77.88, and 75.75, respectively. While for manual tester, they are 85.41, 77.16 and 78.36. The Rockwell hardness of all samples reduce to a large extent after heat treatment. With the same heat treatment, the Rockwell hardness of sample 2 and sample 4 are similar, which is slightly higher than that of sample 3. For each sample, the effect of heat treatment on HRB is the same. The Rockwell hardness of samples exhibits an increase with accelerated cooling at different temperatures. For a fixed cooling rate, different temperature has a same effect on reducing Rockwell hardness of samples.

In summary, the effects of heat treatments on Rockwell hardness are almost consistent with those on Vickers hardness. The only difference is that for the cooling rate of 5°C/min, the effect of reducing the Vickers hardness decreases as temperature increases from 900°C to 1050°C and 1200°C, while the increasing temperature doesn’t exert different influence on the Rockwell hardness.

Table 3.17: Rockwell hardness of sample 2 (automatically measured)

Austenitizing temperature	HRB (Automatic)		
	0.1°C/min	1°C/min	5°C/min
900°C	64.66	68.52	72.86
1050°C	62.41	68.43	72.07
1200°C	63.83	68.28	79.59

Table 3.18: Rockwell hardness of sample 3 (automatically measured)

Austenitizing temperature	HRB (Automatic)		
	0.1°C/min	1°C/min	5°C/min
900°C	61.37	63.69	70.44
1050°C	58.58	64.36	65.96
1200°C	53.86	62.28	69.63

Table 3.19: Rockwell hardness of sample 4 (automatically measured)

Austenitizing temperature	HRB (Automatic)		
	0.1°C/min	1°C/min	5°C/min
900°C	66.23	67.71	74.56
1050°C	65.87	72.99	72.19
1200°C	66.04	64.9	75.63

Table 3.20: Rockwell hardness of sample 2 (manually measured)

Austenitizing temperature	HRB (Manual) 0.1°C/min	 1°C/min	 5°C/min
900°C	68.37	72.66	75.59
1050°C	66.35	72.4	76.54
1200°C	67.03	73.96	80.82

Table 3.21: Rockwell hardness of sample 3 (manually measured)

Austenitizing temperature	HRB (Manual) 0.1°C/min	 1°C/min	 5°C/min
900°C	62.86	71.05	72.82
1050°C	60.63	67.06	68.88
1200°C	53.04	67.6	68.27

Table 3.22: Rockwell hardness of sample 4 (manually measured)

Austenitizing temperature	HRB (Manual) 0.1°C/min	 1°C/min	 5°C/min
900°C	68.88	73.54	76.56
1050°C	66.7	74.88	76.25
1200°C	71.57	71.73	78.34

3.6 Tensile properties

Yield strength (YS), ultimate tensile strength (TS), uniform elongation (UEL) and total elongation (TEL) of all test specimens are summarized in Table 3.23 to Table 3.25 and are plotted in Fig 3.32. After heat treatment, all three samples exhibit a significant reduction in both yield strength and ultimate tensile strength, while they do not experience a considerable change in uniform elongation and total elongation. The effect of temperature and cooling rate on the strength and elongation of three samples are shown in Fig 3.33 and Fig 3.34 in a detailed way respectively.

3.6.1 Yield strength

Among three steels which underwent the same heat treatment, sample 3 always exhibit the lowest yield strength. This can be explained by the contribution from solid solution strengthening, as sample 3 has the lowest concentration of alloy elements among three steels.

The degradation in the yield strength of all samples at 900°C compared to non-heat treated samples can be attributed to the increase in ferrite grain size. At various cooling rates, sample 2, 3 and 4 experience reductions in yield strength, respectively, when temperature increases from 900°C to 1050°C. These reductions in yield strength of three samples can be attributed to not only the loss of strength from grain size strengthening, but a loss of strength contributed by a precipitation hardening mechanism in these steels when they are heat treated at 1050°C and cooled at a fixed cooling rate as well. When steels are heated to 1050°C, which is higher than the eutectoid transformation temperature, the niobium carbides or vanadium carbides begin to dissolve in the austenite phase, while they are not completely dissolved at this temperature, leading to the reduction in precipitation strengthening when the austenite transforms back to ferrite and pearlite in the cooling process. All samples exhibit only a slight decrease in yield strength (when compared with the 1050°C yield strength) when cooled from 1200°C with a cooling rate of 0.1°C/min. At the cooling rate of 1°C/min and 5°C/min, the steels even exhibit slight increase in yield strength when compared with the 1050°C yield strength. This slower trend in strength reduction or even the recovery of the yield strength can be explained by the combined effect of grain size strengthening and precipitation strengthening. At 1200°C precipitates are completely dissolved in the austenite phase, so steels regain strength when cooled from 1200°C due to reprecipitation of niobium or vanadium carbides and nitrides. Meanwhile the ferrite grain size continues to decrease as temperature increases from 1050°C to 1200°C, which leads to a further increase of grain size strengthening. The ferrite grain boundaries and precipitations in the steels have opposite effect on yield strength in this temperature range.

The yield strength of three samples increases with accelerated cooling at different temperatures. This increase in yield strength can be explained by the grain refinement achieved by increasing cooling rate.

3.6.2 Tensile strength

Among three steels, sample 3 has the lowest ultimate tensile strength, while the ultimate tensile strength of sample 4 is the highest before and after the same heat treatment. This can be explained by the volume fraction of pearlite in the microstructure. The pearlite in the microstructure has a strength much higher than that of ferrite. With the same heat treatment, three steels have similar ferrite grain sizes, so the tensile strength contributed by dislocation motion of three steels are more or less the same. Thus, increasing the volume fraction of pearlite has a predominant effect on increasing tensile strength. According to Table, the pearlite volume fraction of sample 4 is the highest among three steels, whereas that of sample 3 is the lowest.

As observed in Fig 3.32 and Fig 3.33, tensile strength of three steels decreases compared to original samples after heat treatment. However, the effect of increasing temperature on reducing tensile strength are not consistent among different samples at various temperatures, which can be attributed to the combined effects of pearlite volume fraction, ferrite grain size and alloying elements.

The tensile strength of three samples increases with accelerated cooling at different temperatures. This indicates that with an increasing cooling rate, grain refinement is achieved and becomes the dominant factor of yield strength, while other factors are only affected a little if any.

In contrast to yield strength, the carbon content or the percentage of pearlite in the microstructure also has an important effect on tensile strength. The ferrite grain distribution is also a factor affecting tensile strength. Additionally, dislocation motion (affected by ferrite grain size and morphology of grain boundaries) and precipitation hardening (affected by alloying elements) are another two determinative factors to tensile strength. It is very important to note that factors such as the initiation of necking in the test specimens also have a significant influence on the ultimate tensile strength. The initiation of necking depends on the strain hardening properties of phases and geometrical imperfections[21]. The influence of necking on the ultimate tensile strength of steels falls outside the scope of the current study.

3.6.3 Elongation

Among three steels, the total elongation of sample 4 is much lower than sample 2 and 3 when being heat treated in the same way. This can be explained by the carbon content of three steels, as total elongation steadily decreases with increasing carbon content. The carbon content of sample 4 is 0.17%, which is almost twice that of sample 2 and 3 (0.08%).

For most heat treatments, there is no consistent effect of temperature or cooling rate on total elongation (ductility), according to Fig 3.32 and Fig 3.33.

Table 3.23: Tensile properties of sample 2

T/°C	CR/°C·min^{-1}	L/mm	T/mm	W/mm	YS/MPa	TS/MPa	UEL	TEL
X	X	75.47	5.53	12.75	400	520	0.15	0.33
900	0.1	76.48	3.76	7.64	314	435	0.15	0.27
900	1	76.20	5.63	10.12	343	467	0.15	0.34
900	5	76.20	5.62	10.12	351	486	0.15	0.33
1050	0.1	75.41	5.70	10.13	267	431	0.15	0.34
1050	1	75.41	5.62	10.12	310	461	0.15	0.33
1050	5	76.99	5.63	10.13	355	504	0.13	0.31
1200	0.1	76.20	4.99	10.13	257	436	0.15	0.31
1200	1	77.06	5.66	10.12	308	470	0.12	0.27
1200	5	76.20	5.62	10.14	359	526	0.11	0.25

Table 3.24: Tensile properties of sample 3

T/°C	CR/°C·min-1	L/mm	T/mm	W/mm	YS/MPa	TS/MPa	UEL	TEL
X	X	75.08	5.13	6.13	400	498	0.15	0.25
900	0.1							
900	1	72.23	5.47	4.82	327	443	0.14	0.31
900	5	73.03	5.01	4.83	335	454	0.14	0.33
1050	0.1	71.44	5.31	4.83	254	391	0.15	0.30
1050	1	72.23	5.30	4.83	270	423	0.15	0.28
1050	5	72.23	5.40	4.83	301	446	0.17	0.28
1200	0.1	72.23	5.22	4.84	246	386	0.14	0.27
1200	1	71.44	4.71	4.85	280	422	0.16	0.31
1200	5	73.03	5.31	4.83	327	471	0.12	0.20

Table 3.25: Tensile properties of sample 4

T/°C	CR/°C·min^{-1}	L/mm	T/mm	W/mm	YS/MPa	TS/MPa	UEL	TEL
X	X	75.70	5.56	6.39	374	541	0.14	0.25
900	0.1	76.20	5.60	3.17	303	449	0.15	0.23
900	1	76.20	5.62	3.17	343	487	0.15	0.20
900	5	76.20	5.59	3.20	351	501	0.16	0.22
1050	0.1	76.20	5.61	3.21	267	459	0.15	0.25
1050	1	76.20	5.93	3.18	310	497	0.15	0.23
1050	5	76.20	5.60	3.20	325	509	0.15	0.23
1200	0.1	76.20	5.52	3.21	269	439	0.15	0.22
1200	1	75.41	5.64	3.19	286	458	0.15	0.23
1200	5	76.99	5.65	3.19	343	512	0.13	0.22

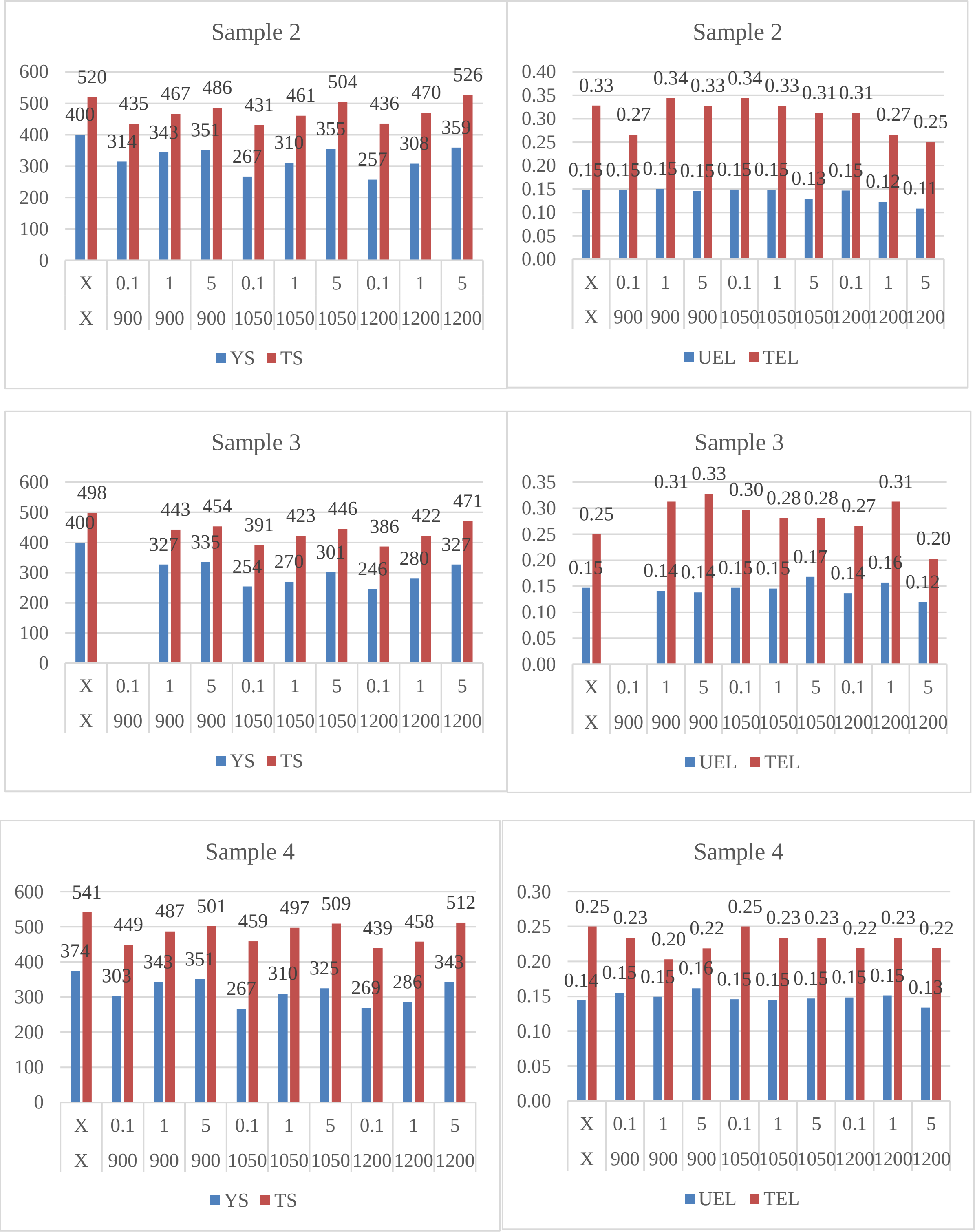

Fig 3.32: Yield strength (YS), tensile strength (TS), uniform elongation (UEL) and total elongation (TEL) of sample 2, 3, 4 after subjected to different temperatures and cooling rates

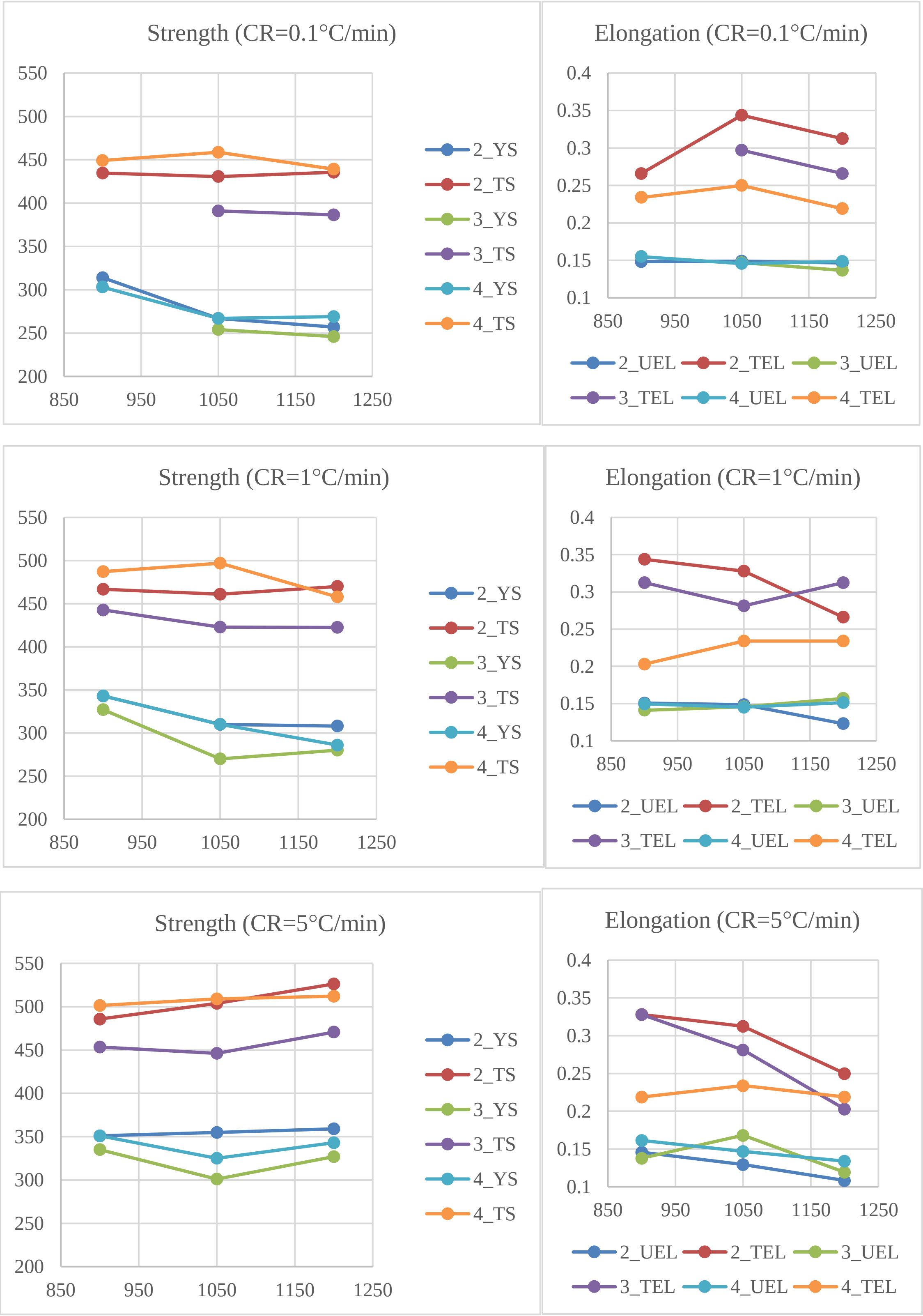

Fig 3.33: The effect of temperature on strength and elongation at various cooling rates

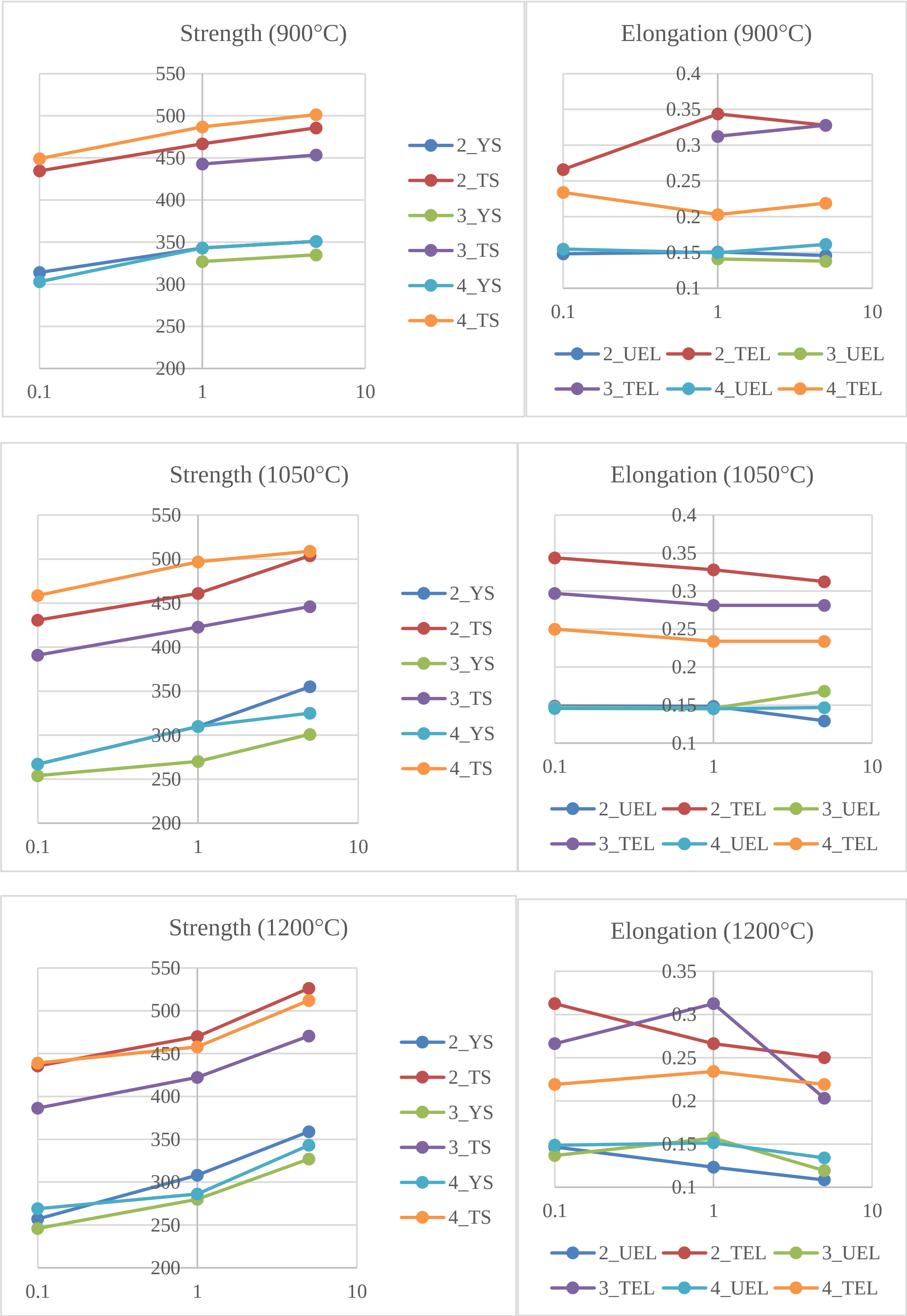

Fig 3.34: The effect of cooling rate on strength and elongation at various temperatures

3.7 Strength prediction

3.7.1 Estimation based on strengthening mechanisms

According to strengthening mechanisms, the yield strength of steel can be increased by one or more of several strengthening mechanisms. These include (1) Solid solution strengthening, (2) Grain size strengthening, (3) Dislocation strengthening, (4) Precipitation strengthening. Then the yield strength can be calculated by the following equation:

$$\sigma_Y = \sigma_0 + \sigma_{SS} + \sigma_{GS} + \sigma_{dis} + \sigma_{ppt} \text{ (MPa)}, \tag{3.5}$$

where σ0 is the intrinsic lattice friction stress (=54 MPa for pure iron single crystal[22, 23]), σ_{SS}, σ_{GS}, σ_{dis}, and σ_{ppt} are contributions from, respectively, solid solution, grain size, dislocation, and precipitation strengthening.

3.7.1.1 Solid solution strengthening

Mechanisms of solid solution strengthening in MA steels are dealt with in detail by Gladman[24]. The contribution of σ_{SS} to σ_Y, based on data provided by Gladman, updated from Pickering and Gladman[25], obtained from regression equations, where the alloying elements are given in weight per cent, can be expressed as

$$\sigma_{SS} = 678P + 83Si + 32Mn + 38Cu + 11Mo \text{ (MPa)}, \tag{3.6}$$

The low weight percentages of Ni and Cr normally present in microalloyed steels provided no contributions to σ_{SS}[26]. The effect of carbon is not considered since the solubility of carbon in ferrite is very low and the pearlite volume fraction does not have any effect on yield strength. According to the chemical compositions, σ_{SS} is thus determined in Table 3.26.

Table 3.26: Solid solution strengthening of three steels

Sample	Elements (wt%)								σ_{SS}
	C	Mn	P	Si	Cu	Mo	V	Nb	(MPa)
2	0.08	1.31	0.016	0.26	0.27	0.04	0.04	0.001	85.49
3	0.08	1	0.01	0.2	0.32	0.04	0.01	0.02	68.32
4	0.17	1.02	0.022	0.14	0.24	0.02	0.032	0.002	68.85

3.7.1.2 Grain size strengthening

The grain size strengthening can be expressed by the Hall-Petch equation[25]:

$$\sigma_{GS} = 15.1d^{-1/2} \text{ (MPa)}, \qquad (3.7)$$

where d is the average grain size of ferrite (in mm) determined by the linear intercept method. Consequently, the values of σ_{GS} are calculated and shown in Table 3.28.

3.7.1.3 Dislocation strengthening

The dislocation strengthening is calculated using the following equation[23, 27]:

$$\sigma_{dis} = 0.38Gb\,\rho^{-1/2} \text{ (MPa)}, \qquad (3.8)$$

where G is the shear modulus of the ferrite (81.6 GPa[22]), *b* is the Burgers vector of the dislocations (0.248 nm[22]), dislocation density is estimated from Vickers hardness measurements. The values of estimated dislocation strengthening are showed in Table 3.29.

3.7.1.4 Precipitation strengthening

The strengthening contribution due to precipitates is determined by the type, size and volume fraction of precipitates in the microstructure. The precipitation strengthening can be estimated by the following equation[23]:

$$\sigma_{ppt} = B\ (\%\text{solute})\ (\text{MPa}), \tag{3.9}$$

where the values of B are presented in Table 3.27[23].

Table 3.27: Coefficient (*B*) of precipitation strengthening, from [23]

Solute and Precipitate	B_{max} (MPa/wt %)	B_{ave} (MPa/wt %)	Solute Concentration (wt %)
V as V_4C_3	1000	500	0–0.15
V as VN	3000	1500	0–0.06
Nb as Nb(CN)	3000	1500	0–0.05
Ti as TiC	3000	1500	0.03–0.18

The concentration of Ti and N being negligible in three steels, σ_{ppt} is determined as 21.5Mpa, 35MPa and 19MPa, respectively, for sample 2, 3 and 4 by considering the average value of the strength coefficient *B* for Nb as NbC precipitates and V as V_4C_3 precipitates. Adding up all the strengthening contributions in the equation of yield strength (Equation 3.5) results in an overall calculated strength. The calculated values of yield strength are shown in Table.

Table 3.28: Grain size strengthening of three steels

Sample	T (°C)	CR (°C/min)	D_α (um)	$D_\alpha^{-1/2}$ (um$^{-1/2}$)	σ_{GS} (MPa)
2	X	X	5.9	0.41	196.59
3	X	X	9.69	0.32	153.40
4	X	X	9.96	0.32	151.30
2	900	0.1	12.98	0.28	132.54
3	900	0.1	15.09	0.26	122.92
4	900	0.1	16.09	0.25	119.04
2	900	1	11.09	0.30	143.39
3	900	1	13.79	0.27	128.59
4	900	1	15.91	0.25	119.71
2	900	5	10.74	0.31	145.71
3	900	5	12.03	0.29	137.67
4	900	5	14.81	0.26	124.08
2	1050	0.1	32.84	0.17	83.33
3	1050	0.1	34.01	0.17	81.88
4	1050	0.1	35.62	0.17	80.01
2	1050	1	24.14	0.20	97.19
3	1050	1	30.25	0.18	86.82
4	1050	1	33.89	0.17	82.02
2	1050	5	23.9	0.20	97.67
3	1050	5	27.12	0.19	91.69
4	1050	5	28.13	0.19	90.03
2	1200	0.1	41	0.16	74.57
3	1200	0.1	45.28	0.15	70.96
4	1200	0.1	41.99	0.15	73.69
2	1200	1	34.85	0.17	80.89
3	1200	1	37.09	0.16	78.41
4	1200	1	38.04	0.16	77.42
2	1200	5	29.41	0.18	88.05
3	1200	5	33.13	0.17	82.96
4	1200	5	34.34	0.17	81.48

Table 3.29: Dislocation strengthening of three steels

Sample	T (°C)	CR (°C/min)	h^* (nm)	ρ (cm^{-2})	σ_{dis} (MPa)
2	X	X	2328.7	6.18E+09	60.46
3	X	X	2563.3	5.62E+09	57.63
4	X	X	2870.7	5.01E+09	54.45
2	900	0.1	2366.6	6.08E+09	59.97
3	900	0.1	3524.5	4.08E+09	49.15
4	900	0.1	3107.5	4.63E+09	52.34
2	900	1	1798.5	8.00E+09	68.80
3	900	1	3958.9	3.64E+09	46.37
4	900	1	1630.7	8.83E+09	72.25
2	900	5	2452.6	5.87E+09	58.91
3	900	5	2562.2	5.62E+09	57.64
4	900	5	1009.6	1.43E+10	91.82
2	1050	0.1	2817.8	5.11E+09	54.96
3	1050	0.1	4495.9	3.20E+09	43.51
4	1050	0.1	1903.2	7.56E+09	66.88
2	1050	1	3232.2	4.45E+09	51.32
3	1050	1	2723.3	5.29E+09	55.91
4	1050	1	1643	8.76E+09	71.98
2	1050	5	3604.7	3.99E+09	48.60
3	1050	5	3080.8	4.67E+09	52.57
4	1050	5	1404.5	1.02E+10	77.85
2	1200	0.1	5018.9	2.87E+09	41.18
3	1200	0.1	4028.2	3.57E+09	45.97
4	1200	0.1	3469.1	4.15E+09	49.54
2	1200	1	2936.7	4.90E+09	53.84
3	1200	1	2515.4	5.72E+09	58.17
4	1200	1	3011.8	4.78E+09	53.16
2	1200	5	2018.9	7.13E+09	64.93
3	1200	5	2183.8	6.59E+09	62.43
4	1200	5	1601.7	8.99E+09	72.90

Table 3.30: Strengthening contributions and predicted yield strength (PYS) of three steels

Sample	T	CR	σ_0	σ_{SS}	σ_{GS}	σ_{dis}	σ_{ppt}	PYS	MYS
2	X	X	54	85.49	196.59	60.46	21.5	418.04	400
3	X	X	54	68.32	153.40	57.63	35	368.34	400
4	X	X	54	68.85	151.30	54.45	19	347.61	374
2	900	0.1	54	85.49	132.54	59.97	21.5	353.51	314
3	900	0.1	54	68.32	122.92	49.15	35	329.39	
4	900	0.1	54	68.85	119.04	52.34	19	313.23	303
2	900	1	54	85.49	143.39	68.80	21.5	373.18	343
3	900	1	54	68.32	128.59	46.37	35	332.28	327
4	900	1	54	68.85	119.71	72.25	19	333.81	343
2	900	5	54	85.49	145.71	58.91	21.5	365.61	351
3	900	5	54	68.32	137.67	57.64	35	352.63	335
4	900	5	54	68.85	124.08	91.82	19	357.75	351
2	1050	0.1	54	85.49	83.33	54.96	21.5	299.28	267
3	1050	0.1	54	68.32	81.88	43.51	35	282.71	254
4	1050	0.1	54	68.85	80.01	66.88	19	288.74	267
2	1050	1	54	85.49	97.19	51.32	21.5	309.50	310
3	1050	1	54	68.32	86.82	55.91	35	300.05	270
4	1050	1	54	68.85	82.02	71.98	19	295.85	310
2	1050	5	54	85.49	97.67	48.60	21.5	307.26	355
3	1050	5	54	68.32	91.69	52.57	35	301.58	301
4	1050	5	54	68.85	90.03	77.85	19	309.73	325
2	1200	0.1	54	85.49	74.57	41.18	21.5	276.75	257
3	1200	0.1	54	68.32	70.96	45.97	35	274.25	246
4	1200	0.1	54	68.85	73.69	49.54	19	265.08	269
2	1200	1	54	85.49	80.89	53.84	21.5	295.72	308
3	1200	1	54	68.32	78.41	58.17	35	293.90	280
4	1200	1	54	68.85	77.42	53.16	19	272.43	286
2	1200	5	54	85.49	88.05	64.93	21.5	313.98	359
3	1200	5	54	68.32	82.96	62.43	35	302.71	327
4	1200	5	54	68.85	81.48	72.90	19	296.24	343

The correlation of the calculated yield strength with the experimental values from the tensile tests are shown in Fig3.35. 28 out of 30 predicted yield strength values are within 15% error range compared to measured yield strength. The calculation correlates well with the experimental values.

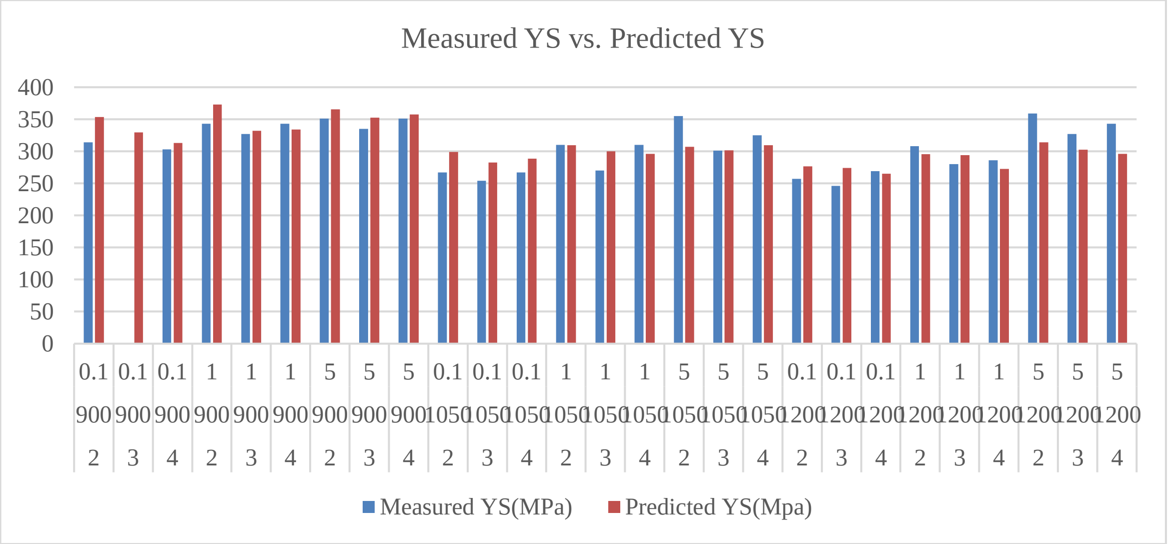

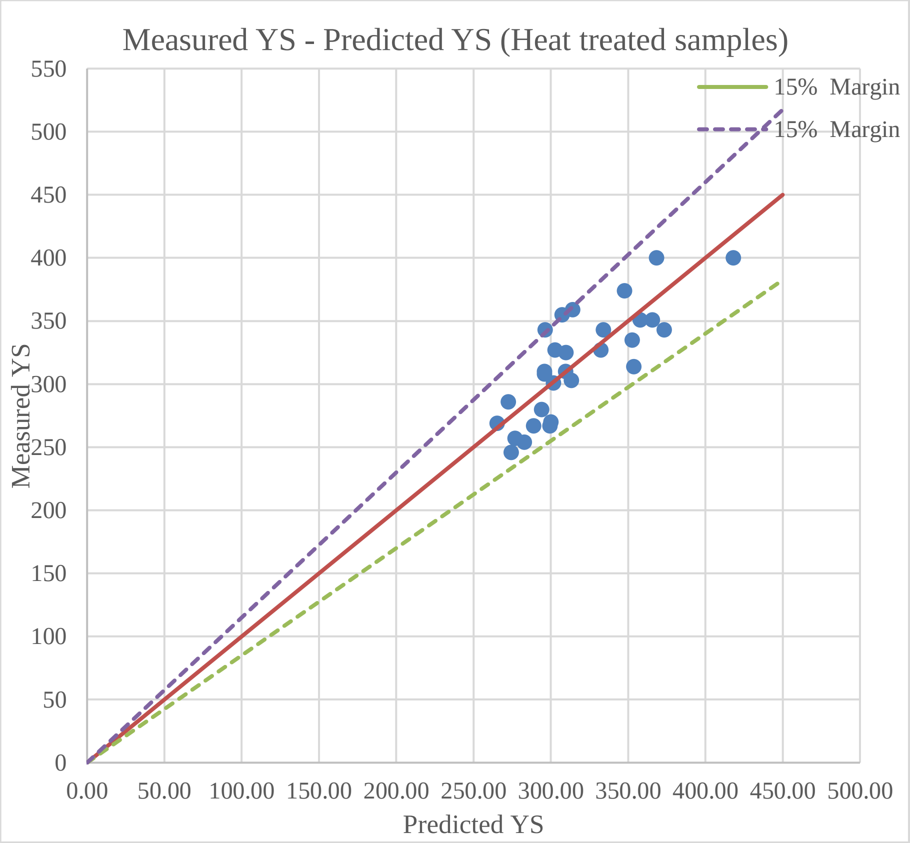

Fig 3.35: Predicted YS vs. Measured YS

3.7.2 Predictive model based on strengthening mechanisms

Based on the strengthening mechanisms and the following calculation, the yield strength of structural steels is dependent on both the chemical compositions and microstructural features. A model is proposed to predict the yield strength of A992 structural steels that are subjected to different heat treatments.

The predictive model takes the chemical composition into account by assuming that A992 structural steels have the similar Nitrogen content with those provided in the Mill Certificate (0.01%). Now the solid strengthening becomes:

$$\sigma_{SS} = 678P + 83Si + 32Mn + 38Cu + 11Mo + 5544N \text{ (MPa)}, \tag{3.10}$$

Since the dislocation density of steels were estimated based on the indentation size effect, and not enough different loads were applied to obtain an accurate characterization of dislocation strengthening, σ_{dis} is not included in this model.

By fitting Equation 3.1-3.4 into Equation 3.7, the grain size strengthening can be expressed by:

$$\sigma_{GS} = 15.1(0.001*\exp(0.92 + 0.44\ln D_\gamma - 0.1\ln CR))^{-1/2} \text{ (MPa)}, \tag{3.11}$$

where D_γ = austenite grain size (um); and CR = cooling rate (°C/s). D_γ is dependent on the chemical composition of the steels.

For Vanadium Microalloyed steels:

$$D_\gamma = 0.4686T - 407.36 \tag{3.12}$$

For Niobium Microalloyed steels:

$$900\text{-}1050°C: D_\gamma = 0.1688T - 135.73 \tag{3.13}$$

$$1050\text{-}1275°C: D_\gamma = 0.8444T - 853.29 \tag{3.14}$$

where D_γ = austenite grain size (um); and T = temperature (°C)

By fitting all these strengthening contributions into Equation 3.5, the predicted yiled strength is expressed by:

$$\sigma_Y = 54 + (678P + 83Si + 32Mn + 38Cu + 11Mo + 5544N) + 15.1(0.001*\exp(0.92 + 0.44\ln D_\gamma - 0.1\ln CR))^{-1/2} + (1500Nb + 500V)\ (MPa), \quad (3.15)$$

The yield strengths obtained from the tensile tests and the predictive model are compared in Fig 3.36. As observed, the proposed model is able to predict reasonably close yield strength when compared to experimental values.

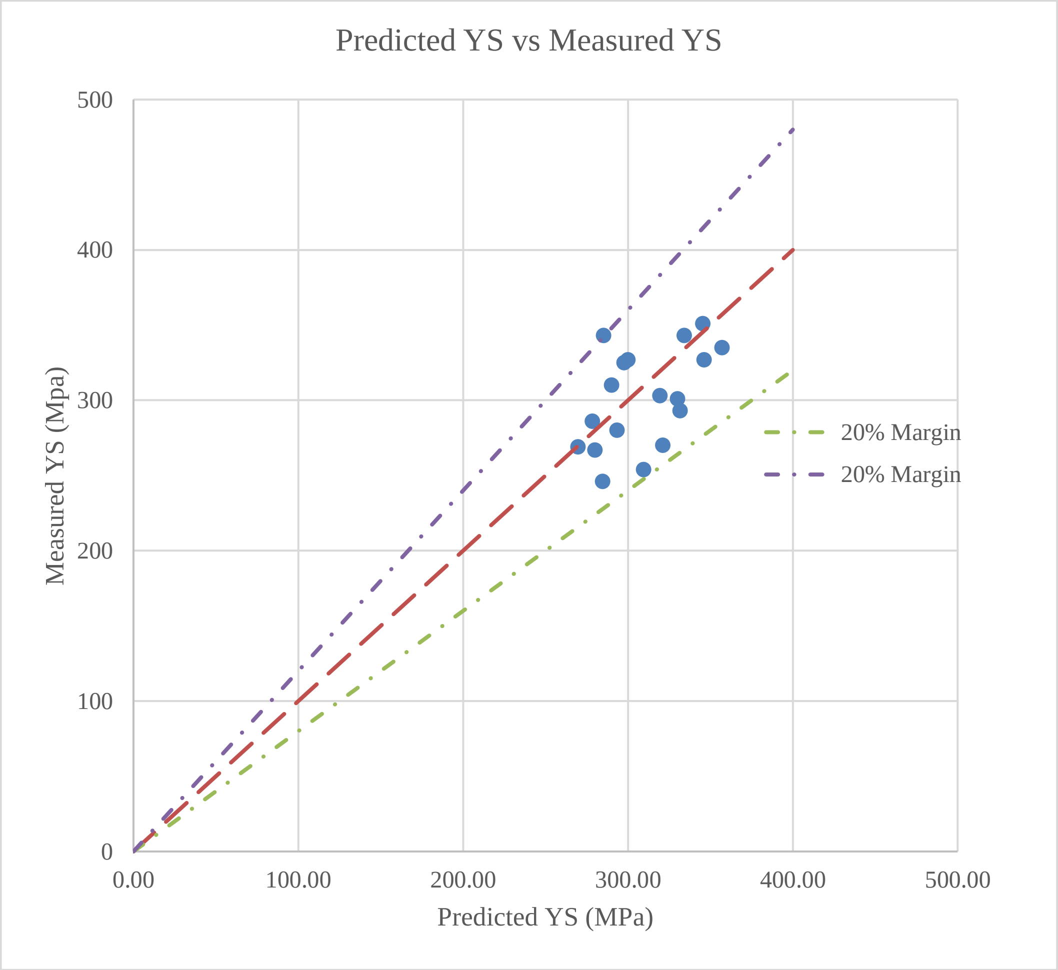

Fig 3.36: Predictive results of the yield strength

Chapter 4

Conclusions

In order to enhance the seismic performance of steel moment connections, an innovative idea which reduces the strength of beam flanges by heat treatments was presented. When applying this concept to achieve a certain level of strength for a given type of steel, the heat treatment parameters need to be determined and was the main focus of this research. The aim of the study is achieved through microstructural studies, mechanical testing and by taking advantage of strength-property relationships. A992 structural steels are selected in this work.

1. Original microstructures of A992 steels are studied. Ferrite-pearlite microstructures are observed in all steels. Sample 2 has the smallest ferrite grain size, which, in addition to other factors during processing can be attributed to its higher Mn content, which lowers the austenite transformation temperature, resulting in ferrite grain refinement . Sample 4 has the highest pearlite volume fraction, which is attributed to its highest carbon concentration.
2. The grain growth behavior of austenite is studied. The austenite grains become larger as temperature increases, while the austenite grain growth has almost stopped after the samples are held for over 10 minutes. Austenite grains grow in a linear manner with increasing heating temperature for both sample 3 and sample 4. The austenite grain growth of sample 4 is consistent in temperature range from 900°C to 1275°C, while

there is a turning point at 1050°C on sample 3's grain growth curve. This is attributed to the different solubility of NbC and VC in the austenite phase. Based on the data, two regression equations are proposed to predict the austenite grain growth of sample 3 and sample 4 with reasonable accuracy.

3. In the ferrite grain growth study, the ferrite grain size increases with an increase in austenite grain size, while ferrite grain refinement is achieved with an increase in cooling rate. The temperature and cooling rate doesn't affect pearlite volume fraction. Modification is made to the Saito's equation to predict ferrite grain growth based on prior austenite grain size and cooling rate. The calibrated equation correlates well with experimental values. EBSD analysis is conducted to study ferrite grain distribution. At 1050°C and 1200°C, the microstructure of steels loses some unimodality and there's an increase in spread of the grain size distribution when compared to the non-heat treated steels and those treated at 900°C, which are consistent with optical microscopy observations.
4. Vickers hardness of steels experience an obvious reduction after being heat treated. Among heat-treated steels, HV increases with an increasing cooling rate, while HV doesn't exhibit considerable change when temperature increases. Rockwell hardness testing indicates similar results. Neither HV nor HRB is a good indicator of ferrite grain size. Dislocation density is estimated based on indentation Vickers hardness tests with different loads.
5. After heat treatment, steels exhibit a reduction in both yield strength and ultimate tensile strength, while they do not experience a considerable change in uniform

elongation and total elongation. Sample 3 has the lowest yield strength. This can be explained by the contribution from solid solution strengthening, as sample 3 has the lowest concentration of alloy element. As temperature increases, the change in yield strength can be attributed to the combined effect of grain size strengthening and precipitation hardening. When temperature increases from 900°C to 1050°C, the loss of strength is contributed by both grain size coarsening and loss of precipitation strengthening. When temperature continues to increase above 1050°C, ferrite grains continues to grow while the steels regain strength from the reprecipitation of niobium and vanadium carbides, which slows down the decrease of yield strength or even leads to the recovery of yield strength. The increase of yield strength with accelerated cooling is attributed to the grain refinement. Before and after the same heat treatment, sample 3 always has the lowest ultimate tensile strength, while that of sample 4 is the highest. This is explained by the significant difference of pearlite volume fractions in the microstructure. The effect of temperature on tensile strength is different, which is a combined effect of pearlite volume fraction, ferrite grain size and alloying elements. The increase of tensile strength with accelerated cooling is mainly caused by the grain refinement. The total elongation of sample 4 is the lowest with the same heat treatment, as it has the highest carbon content, which significantly reduces the ductility of steels.

6. The yield strength of all original and heat-treated A992 steels is estimated through the evaluation of individual strengthening contributions, including lattice friction, solid solution strengthening, grain size strengthening, dislocation strengthening and precipitation strengthening. The calculated yield strength correlates well with the

experimental values. Moreover, a model is proposed based on strengthening mechanisms with given chemical compositions and heat treatment parameter, and is able to predict reasonably close yield strength.

Chapter 5

Future work

The following research fields are recommended to be pursued:

1. Since neither Vickers hardness nor Rockwell hardness is a good indicator of yield strength, some other types of hardness testing (such as Brinell hardness) need to be conducted.
2. All the estimation and prediction of strength is based on the assumption that the chemical compositions of steels are not affected by the heat treatments. However, the chemical composition of steels after heat treatment needs to be quantitatively characterized considering the effect of oxidation and diffusion.
3. To accurately calculate the precipitation strengthening, TEM method needs to be used to characterize the size and volume fraction of precipitates. TEM is also a more accurate method of measuring dislocation density compared to the estimation based on indentation size effects.

References

[1] https://www.eurocode.us/earthquake-resistance-eurocode-8/capacity-design-principle.html

[2] FEMA, December. "Earthquake-Resistant Design Concepts." *Washington DC* (2010).

[3] Paulay, Thomas. "The philosophy and application of capacity design." *Scientia iranica* 2.2 (1995): 117-143.

[4] Ali, Shamshad , Farhan Malik, Tanmay Sonone, Bhushan Kalbande, and Harshala Agale. "Analysis of building with soft storey during earthquake." *Int. Res. J. Eng. Technol.(IRJET)* 4.3 (2017): 1005-1009.

[5] Ye, Lieping, and Zhe Qu. "Failure mechanism and its control of building structures under earthquakes based on structural system concept." *Journal of Earthquake and Tsunami* 3.04 (2009): 249-259.

[6] Muto, Matthew, and Swaminathan Krishnan. "Hope for the best, prepare for the worst: Response of tall steel buildings to the shakeout scenario earthquake." *Earthquake Spectra* 27.2 (2011): 375-398.

[7] Engelhardt, M. D. and Sabol, T. A. (1997), Seismic-resistant steel moment connections: developments since the 1994 Northridge earthquake. Prog. Struct. Engng Mater., 1: 68–77.

[8] Morrison, Machel. " Innovative Seismic Performance Enhancement Techniques for Steel Building Moment Resisting Connections." (2015): 441-451.

[9] Morrison, Machel, Doug Schweizer, and Tasnim Hassan. "An innovative seismic performance enhancement technique for steel building moment resisting connections." *Journal of Constructional Steel Research* 109 (2015): 34-46.

[10] Mohandas, Kiran , Shahab Ramhormozian, G. Charles Clifton, and Gregory Anthony MacRae. "The seismic performance of structural steel buildings in the 2010/2011 Christchurch Earthquake series and the 2016 Kaikoura earthquake: lessons learned, ongoing research and needs of industry." (2020).

[11] Johnson, Matthew Q., and J. E. Ramirez. *Preliminary evaluation of heat affected zone toughness in structural shapes used in the construction of seismic moment frames*. SAC Joint Venture, 2002.

[12] Jaquess, Timothy Kyle, and Karl H. Frank. *Characterization of the material properties of rolled sections*. SAC Joint Venture, 2002.

[13] ASTM. "Standard specification for structural steel shapes." West Conshohocken, PA: ASTM, 2015.

[14] Santella, M. L., "Grain Growth and High-Temperature Hot Rolling Behavior of Low Alloy Steel Austenite", Ph.D. Thesis, University of Pittsburgh, 1981, pp 49-52.

[15] ASTM E92-17. "Standard test methods for vickers hardness and knoop hardness of metallic materials." *West Conshohocken (PA): ASTM International* (2017).

[16] Nix WD, Gao H. J Mech Phys Solids 1998;46:411–25.

[17] Graça, S ., R. Colaço, P. A. Carvalho, and R. Vilar. "Determination of dislocation density from hardness measurements in metals." *Materials Letters* 62.23 (2008): 3812-3814.

[18] Lavigne, Olivier, Andrei Kotousov, and Vladimir Luzin. "Microstructural, mechanical, texture and residual stress characterizations of X52 pipeline steel." *Metals* 7.8 (2017): 306.

[19] T. Gladman: *The Physical Metallurgy of Microalloyed Steels*, The Institute of Materials, London, UK, 1997.

[20] Saito, Y., Tanaka, M., Sekine, T. and Nishizaki, H., "Mechnical Properties control in Controlled Rolling and Accelerated Cooling of HSLA Steels", Proc. High Strength Low Alloy Steels, University of Wollongong, Wollongong. Australia, 1985, pp. 28-32.

[21] Sajid, Hizb Ullah, Dayakar L. Naik, and Ravi Kiran. "Microstructure–Mechanical Property Relationships for Post-Fire Structural Steels." *Journal of Materials in Civil Engineering* 32.6 (2020): 04020133.

[22] Kamikawa, N.; Sato, K.; Miyamoto, G.; Murayama, M.; Sekido, N.; Tsuzaki, K.; Furuhara, T. Stress-strain behavior of ferrite and bainite with nano-precipitation in low carbon steels. *Acta Mater.* **2015**, *83*, 383–396.

[23] Liu, G. Designing with Carbon-, Low-, and Medium-alloy Steels. In *Handbook of Mechanical Alloy Design*; Totten, G.E., Xie, L., Funatani, K., Eds.; Taylor & Francis Inc., Marcel Dekker Inc.: New York, NY, USA, 2004; pp. 73–89.

[24] T. Gladman: 'Microalloyed steels'; 1997, London, Institute of Materials.

[25] F. B. Pickering and T. Gladman: ‘An investigation into some factors which control the strength of carbon steels’ ‘Metallurgical developments in carbon steels’, Special Report 81, 11–20; 1963, London, ISI.

[26] Baker, T. N. "Microalloyed steels." *Ironmaking & Steelmaking* 43.4 (2016): 264-307.

[27] Yang, J.R.; Bhadeshia, H.K.D.H. The dislocation density of acicular ferrite in steel welds. *Weld. Res. Suppl.* **1990**, *69*, 305s–307s.